FISEVIER

Contents lists available at ScienceDirect

Journal of Volcanology and Geothermal Research

journal homepage: www.elsevier.com/locate/jvolgeores



Geochemistry of vapor-dominated hydrothermal vent deposits in Yellowstone Lake, Wyoming



Amanda Tudor ^a, Andrew Fowler ^a, Dionysis I. Foustoukos ^b, Bruce Moskowitz ^a, Liheng Wang ^c, Chunyang Tan ^{a,*}, William E. Seyfried Jr ^a

- ^a University of Minnesota, Department of Earth and Environmental Sciences, Minneapolis, MN 55455, United States
- b Carnegie Institution of Washington, Earth and Planets Laboratory, 5241 Broad Branch Road, NW Washington, DC 20015-1305, United States
- ^c Key Laboratory of Shale Gas and Geoengineering, Institute of Geology and Geophysics, Chinese Academy of Sciences, Beijing 100029, China

ARTICLE INFO

Article history: Received 7 January 2021 Received in revised form 8 March 2021 Accepted 9 March 2021 Available online 19 March 2021

Keywords: Yellowstone Lake Hydrothermal deposits Vent fluid chemistry Mineral alteration Reaction rates

ABSTRACT

Yellowstone Lake hydrothermal vent systems have been studied using ROV assets to better understand the chemical and mineralogical evolution of the sublacustrine sediments through which the hot spring fluids discharge to the lake floor. Here we focus on the deposits/alteration and coexisting vent fluid chemistry associated with the Deep Hole on the lake floor, east of Stevenson Island. Remote in its location, at 120 m below the lake surface, this region in the northeast portion of Yellowstone Lake is associated with numerous hydrothermal vents and hot springs, providing evidence of high-temperature fluid-mineral interaction and phase separation phenomena. Vapor-dominated hydrothermal fluids issuing from Deep Hole vents attain temperatures in excess of 150 °C and are enriched in magmatically derived H₂S and CO₂. Upon mixing with lake water in the root zone of the hydrothermally active vents, the dissolved gases render the mixed fluid, both acidic and reducing, effectively transforming diatomaceous sediment, with detritally sourced Al and Fe components, to an alteration assemblage dominated by kaolinite, pyrite, and lesser boehmite. These alteration processes have been modeled by computer based simulations, coupling fluid flow and mineral dissolution kinetics, to provide insight on the temporal evolution of the vent system. Results predict rapid dissolution of amorphous silica. The magnitude and rate of silica loss, facilitated by the continuous influx of acidic source fluids, yields an increasingly silica poor alteration mineral sequence with time, characterized by quartz, followed by kaolinite and ultimately boehmite. These data are consistent with the observed decrease in SiO₂/Al₂O₃ ratio of the vent deposits with increasing abundance of trace immobile elements, suggesting significant mass loss with reaction progress. Pyrite is predicted to form from sulfidation of magnetite, with noteworthy decrease in magnetic intensity, as measured for hydrothermally altered sediment in the near-field vent environment. Moreover, hydrogen isotope compositional data for kaolinite, together with δD vent fluid data, suggest temperatures in keeping with the high temperatures measured for the vent deposits and discharging fluid, while supporting the potential use of kaolinite as a geothermometer. The predicted and observed transformation of silica-rich protolith to kaolinite, boehmite, and pyrite underscores the large scale dissolution and removal of silica, with possible implications for the temporal evolution of vent deposits on the lake floor in the Stevenson Island Deep-Hole region.

Published by Elsevier B.V.

1. Introduction

Yellowstone National Park (YNP) (Wyoming, USA) has long been recognized as a region of unusually intense volcanic and tectonic activity that is currently centered above the Yellowstone hotspot (Morgan et al., 2009a). Concentrated within the boundaries of the most recent expression of this hotspot—0.64 Ma Yellowstone Caldera—heat and non-condensable gases from the underlying crystallizing magma reservoir interact with deeply circulating meteoric water to produce

* Corresponding author. E-mail address: Tanc@umn.edu (C. Tan). extensive and geochemically diverse expressions of hydrothermal activity (Fournier, 1989; Chiodini et al., 2012; Hurwitz and Lowenstern, 2014). Largely recognizable, the subaerial geothermal systems of YNP have been extensively studied; however, less is known of the sublacustrine hydrothermal systems of Yellowstone Lake (Shanks III et al., 2007; Fowler et al., 2019b).

Straddling the southeast margin of the 0.64 Ma Yellowstone Caldera, the northern two-thirds of Yellowstone Lake (Fig. 1A), is hydrothermally active, and accounts for ~10% of the total flux of hydrothermally derived components into Yellowstone National Park (YNP) overall (Morgan and Shanks, 2005). The 341 km² basin is composed largely of Quaternary rhyolitic flows, glacial deposits, and lake sediment; with

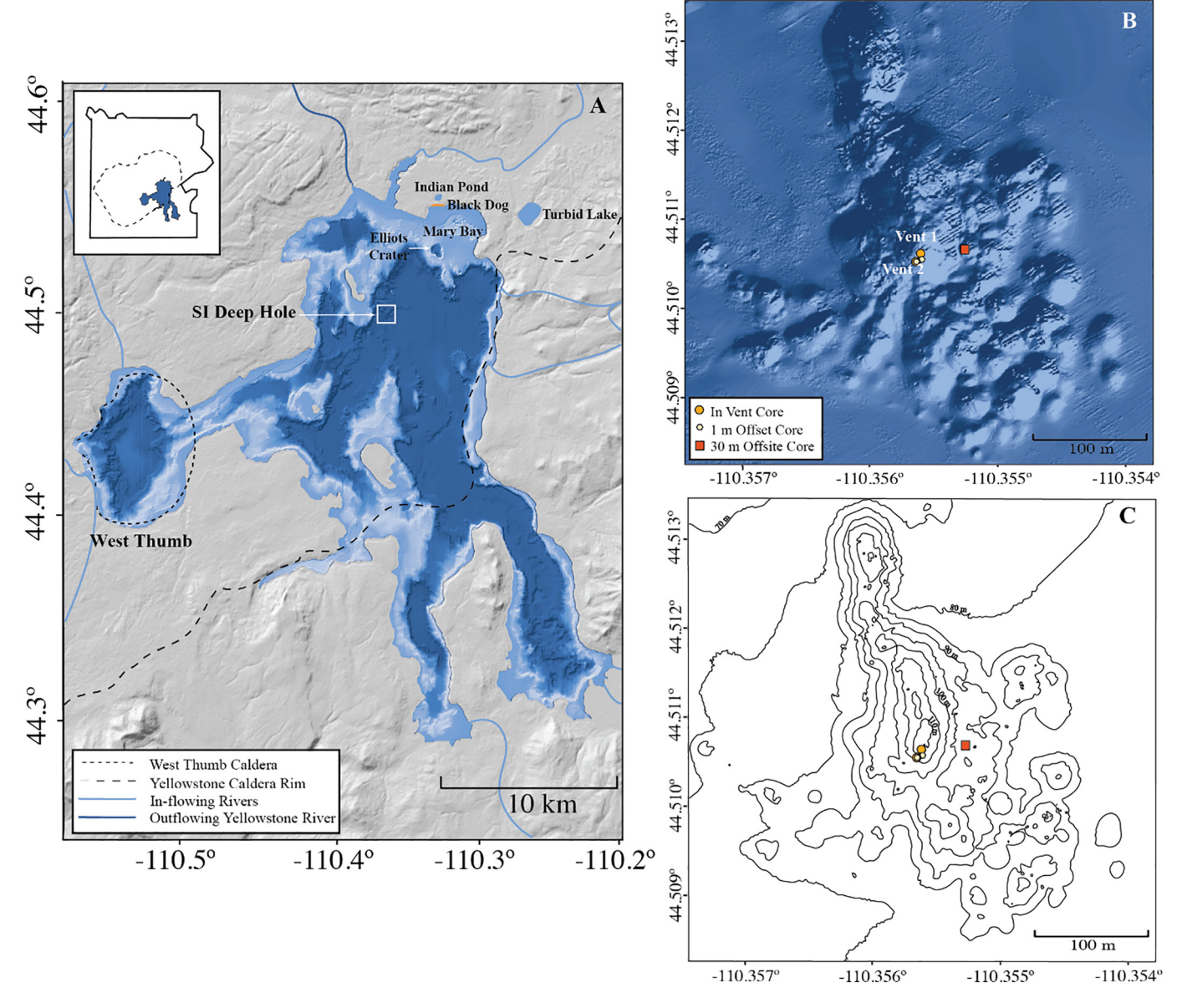
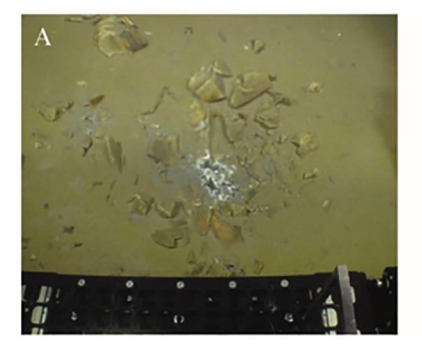


Fig. 1. Location of SI Deep Hole and associated vents in Yellowstone Lake, Wyoming. (A) Yellowstone Lake with bathymetric lake-wide data from (Morgan et al., 2007a; Morgan et al., 2007b). Caldera margins from (Christiansen, 2001). North basin hydrothermal areas from Morgan et al., (2007a). (B) Stevenson Island Deep Hole vent field showing location of vent sites 1 and 2. These sites were instrumented for long-term monitoring of vent fluid temperature and chemistry (Tan et al., 2020). Push core samples reported in the present study were also obtained in and around vent sites 1 and 2. (C) Stevenson Island Deep Hole vent field bathymetry with depth contour lines. SI Deep Hole AUV data from (Sohn et al., 2017). The yellow symbols designate the location of vents 1 and 2, while the red square shows the site of the least altered sediment sampled.

the upper sequence of unaltered basin floor primarily consisting of laminated fine-grained lacustrine sediments. These sediments contain significant amounts of diatomaceous material (Johnson et al., 2003; Morgan et al., 2009b), and include evidence of hydrothermal explosions and hydrothermal activity sufficient to alter the basin morphology (Shanks III et al., 2007). As recently emphasized from high-resolution, multi-scale surveys, hydrothermal activity within the lake is well recognized by magnetic lows within lake floor vent depressions, including linear fissures southeast of Stevenson Island (Bouligand et al., 2020). These northwestern trending fissures, also recognized from ROV observations, and earlier from high-resolution bathymetric data (Johnson et al., 2003; Morgan et al., 2009b), likely focus flow of more deeply sourced hydrothermal fluids, enhancing near-surface alteration, especially in the Deep Hole area, east of Stevenson Island (SI Deep Hole) (Fig. 1B, C). At ~120 m depth, fluids issuing from this region of the

lake floor produce a recognizable thermal anomaly in the lake water column, which suggests a hydrothermal fluid influx of $\sim \! 1.4 \times 10^3$ kg/s and heat flux of 20–50 MW (Sohn et al., 2019). The individual hydrothermal vents present within SI Deep Hole, are among the hottest sub-lacustrine vents to be reported anywhere in the world, with insitu temperatures of 174 °C (Fowler et al., 2019b). Described as 5–10 cm non-constructional orifices (Fig. 2A), SI Deep Hole hydrothermal vents issue fluids that not only achieve high temperatures but are also CO₂ saturated, as suggested by thermodynamic calculations and the observations of CO₂ bubbles separating from fluids issuing from vents on the lake floor (Fowler et al., 2019b; Tan et al., 2017).

The unique nature of the composition and temperature of the venting fluid is suggestive of a steam-heated hydrothermal system (White et al., 1971; Fowler et al., 2019b). Thus, the SI hydrothermal vent fluids in the Deep Hole region are mixtures of high enthalpy



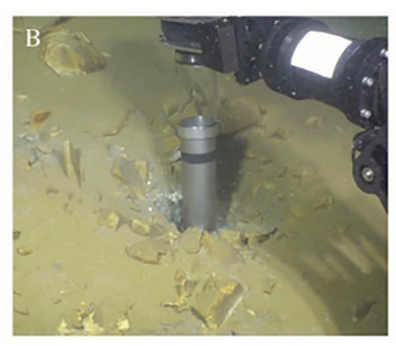




Fig. 2. Hydrothermal vents on the floor of Yellowstone Lake are relatively small (~10 cm in width), non-constructional features characterized by diffusive discharge of hot fluids (A). Although unusually hot, the vapor-dominated vent fluids lack dissolved components sufficient to form sulfide chimneys or silica spires at the lake floor (Fowler et al., 2019a, 2019c). The white colour adjacent to the area of active venting is a result of microbial activity. ROV preparing to deploy push core at Vent site 1 (B). Push core deployment and recovery (C) is made possible by a ball-handle on the ROV manipulator, facilitating insertion and removal of the sediment cores. The clear PVC "window" toward the top of the core confirms successful sampling.

steam and lake bottom water (Fowler et al., 2019b) (Fig. 3). The occurrence of a vapor-dominated hydrothermal system is possible due to an overlying low-permeability substrate acting as a sediment cap to a more permeable reservoir. In general, a sediment cap of low permeability allows steam to escape, while minimizing the influx and quench effects of the ambient lake water (Schubert et al., 1980; Raharjo et al., 2016). Thus, the high enthalpy vapor transfers heat by conduction and advection to the overlying lake water, broadly similar to heat transfer processes of subaerial fumaroles observed elsewhere in YNP (Hurwitz and Lowenstern, 2014). Vapor-dominated subaerial systems are often recognized by noteworthy acidity and high sulfate concentrations (Rowe et al., 1973; Truesdell and White, 1973; Hurwitz and Lowenstern, 2014;. This is not the case, however, for sub-lacustrine Stevenson Island vent fluids owing to the general absence of dissolved O₂, and thus, acidity is provided not from sulfide oxidation, but rather hydrolysis of dissolved CO₂ (Sohn et al., 2017; Fowler et al., 2019b). Accordingly, sub-lacustrine hydrothermal systems at Stevenson Island in Yellowstone Lake might provide a better representation of chemical reactions that may occur within subaerial systems, but at depths hundreds of meters below the land surface (Fowler et al., 2019b, 2019c).

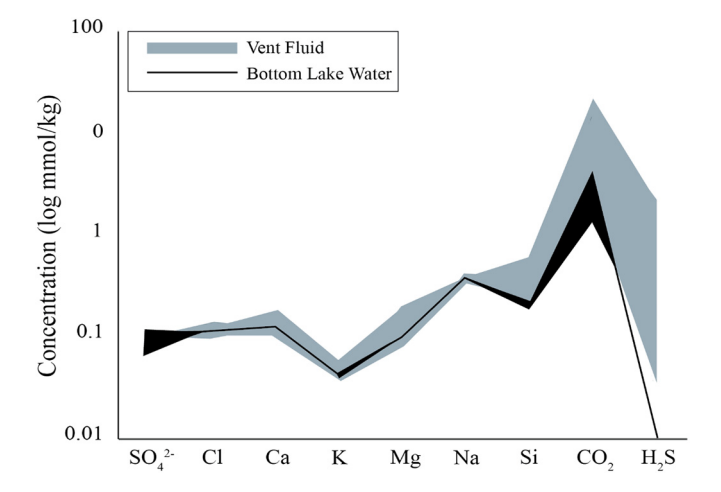


Fig. 3. Chemical composition of SI Deep Hole vent fluids compared with Yellowstone Lake bottom water. The noteworthy increases in magmatically derived CO_2 and H_2S and the relative lack of change of other lake water components are consistent with a vapor-dominated hydrothermal system (Fowler et al., 2019b, 2019c). The addition of highenthalpy steam to lake water in pores and fractures in sublacustrine sediments below the lake floor is fundamentally responsible for heat and mass transfer processes.

Here we focus on the composition of minerals sampled from active and inactive vents in the SI area on the floor of Yellowstone Lake. To accomplish this, we use chemical, mineralogical, isotopic, magnetic, and in-situ temperature data, as well as results of 1D numerical simulations, depicting mineral alteration processes and rates of mass transfer. In combination with previously reported vent chemistry (Fowler et al., 2019b, 2019c), these data provide a comprehensive picture of the chemical and mineralogical evolution of the Stevenson Island sublacustrine hydrothermal system in time and space.

2. Methods

2.1. Field methods and sample processing

2.1.1. Field methods

Sediment sampling was conducted in August of 2017 and 2018. Sampling lake floor vent deposits was challenging, but accomplished by use of the remotely operated vehicle (ROV) "Yogi" and support ship (R/V Annie), operated by the Global Foundation for Ocean Exploration. Equipped with a 5-function electric manipulator arm for fluid and sediment sampling, 9000 lm LED lights, and multiple high definition cameras, ROV "Yogi" was able to obtain sediment samples through the use of push corers. The push corers were specially designed by the Global Foundation for Ocean Exploration, and consist of 2-in, diameter stainless steel tubes attached by ball-handle to the ROV manipulator arm (Fig. 2B, C). Push core samples, measuring 6-22 cm in length, were obtained from several localities in the vent and near vent region of the lake floor at SI Deep Hole. Cores: YL17U03, YL17U04 and YL17U01, YL17U02 were acquired from active vent sites 1 and 2, respectively (Fig. 4). Additionally, a single push core (YL17U05) was taken approximately 30 m from the active venting area (Fig. 1B, C) and served as reference against which more altered sediments at/near vent sites could be compared. Upon return to R/V Annie, the samples were transferred to a freezer on the vessel and stored in polycarbonate containers. Samples were later processed at the National Science Foundation (NSF) LacCore facility at the University of Minnesota (UMN).

2.1.2. Sample processing

Cores were first split in half with a medical cast saw to reveal mineralogical and textural characteristics more clearly. Digital images were obtained with a Deutsche Montan Technologie DMT Colour CoreScan system, which processes images by line-scan charged-coupled device (CCD) camera (Fig. 4). Inherently heterogeneous cores were then subsampled in the UMN Geochemistry Laboratory to acquire a spatially broad geochemical perspective. This includes sampling material from the bottom (B), middle (M), and top (T) of the respective cores. Cores

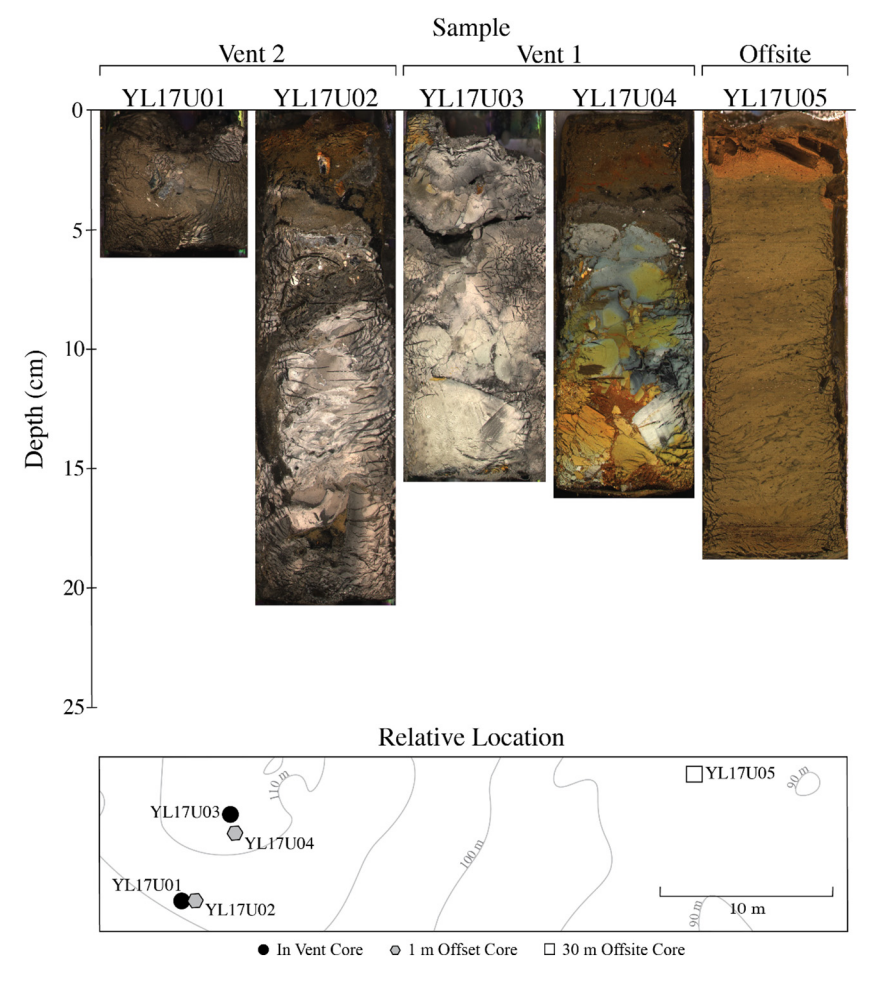


Fig. 4. Photographic images of push cores from the SI Deep-Hole region that were recovered from both active (YL17U01, YL17U03) and inactive vent areas (YL17U02, YL17U04). The so-called inactive sites are offset ~1 m from sites of active fluid discharge. Temperature measurements at both sites indicate relatively high temperatures (Tan et al., 2020). The core samples display depth and textural characteristics, while the relative location of the cores on the lake floor is depicted in the bottom panel. Core YL17U05 was obtained a distance of approximately 30 m from vent 1 and vent 2 sites. Subsamples of cores from all sites were analyzed chemically, mineralogically, isotopically (D/H), and for magnetic intensity.

taken from active vent sites were subsampled at an even finer scale to provide a better understating of compositional variability with core depth. Offset cores (~1 m displaced from the vent) display vertical variability and thus were subsampled in a number of locations within the core. Additional subsamples were collected to determine the magnetic intensity and hydrogen isotope composition of selected alteration minerals.

2.2. Geochemical data

2.2.1. Major and trace element chemistry

Eight core-derived hydrothermally altered sediments from multiple localities were analyzed by ICP-MS (Inductively Coupled Plasma -Mass Spectrometry) and ICP-OES (Inductively Coupled Optical Emission Spectrometry) at UMN. The sediment samples were digested in HF-HCl-HNO $_3$ at high temperature and high pressure using a titanium supported Teflon lined reactor (Cotta and Enzweiler, 2012). Analytical uncertainty from replicate measurements were generally $\pm 5\%$ for reported concentrations of major elements and $\pm 10\%$ for selected trace elements.

The total sulfur concentration of sediment samples (reported as SO₃) was determined by using a Spectro-XEPOS benchtop X-ray Fluorescence EDS spectrometer at the Carnegie Institution of Washington-Earth and Planets Laboratory. Laboratory protocols have been developed to analyze powdered samples (>0.2 g) from a wide range of ultramafic,

mafic and felsic lithologies. Accuracy was constrained by analyzing international reference materials W1, G2 and DTS-1, with precision assessed by repeat analyses of the standards in different sample batches (Guice et al., 2021). Duplicate measurements display standard deviations (1 σ) of up to $\pm 0.3\%$.

2.2.2. Deuterium/hydrogen stable isotopes

The elemental and isotope hydrogen analyses of structural water in altered sediments was performed at the Carnegie Institution of Washington, Earth and Planets Laboratory by utilizing a Thermo Finnigan DeltaPlus XL mass spectrometer connected to a Thermo Finnigan Thermal Conversion elemental analyzer (TC/EA) operating at 1400 °C. The protocols for H_2O analysis in silicate minerals by IRMS-TC/EA have been benchmarked with solid-state 1H Nuclear Magnetic Resonance spectroscopy in hydrous alumino–silicate glasses (Cody et al., 2020).

Prior to the analysis, samples were dried at 90 °C for 7 days. The samples were then placed in an auto sampler and flushed with zero-grade, dry He for 2 h to remove H_2O that was adsorbed from the atmosphere during the transfer from the dry furnace to the auto sampler. H_2 reference gas of known δD composition (-123.39% SMOW) was used for standardization. Calibrations were performed with internal working gas standards derived from the reference gas and analyzed at regular intervals to monitor the accuracy of the measured isotopic ratios and elemental compositions throughout the run. In-house solid standards were

calibrated against international (SMOW, NBS-22, air) and commercially certified standards from Isoanalytical, USGS, NBS, and Oztech. An H3+ correction was determined and applied to the hydrogen measurements (Sessions et al., 2001). Hydrogen stable isotope data are reported in standard delta notation (δA) expressed as:

$$\delta A() = \left[\frac{(R_S - R_{STD})}{R_{STD}}\right] \times 1000 \tag{1}$$

where RS and RSTD are the isotope ratios of the sample and the standard, respectively.

Isotopic and elemental analysis uncertainties correspond to a standard deviation (1σ) between replicate analyses of distinct subsamples (n>2). Replicate samples were analyzed sequentially to check for both sample heterogeneity and small memory effects that are known to occur. Blanks were also run before and after each sample to minimize memory effects. Measured analytical uncertainty varies from $\pm 0\%$ to $\pm 0.4\%$, dependent on the sample. For the H₂O analysis uncertainty did not exceed $\pm 0.4\%$ for any samples.

2.3. Mineralogical analysis

Mineralogy of altered sediment samples was determined by a Rigaku MiniFlex, X-Ray Diffractometer (XRD) in the Department of Earth and Environmental Sciences at UMN. These same samples were also studied using Hitachi TM1000 Scanning Electron Microscope (SEM), at the NSF-LacCore facility to determine the presence of accessory minerals. XRD measurements, with the exception of YL17U02M, were measured on bulk sediment sample separates. Fines from YL17U02M were separated by gravitational settling in water to obtain a more concentrated clay fraction of an SI Deep Hole sample. To confirm the kaolinite-rich nature of all samples, sediments were subjected to both heating (550 °C for 2 h) and treatment with ethylene glycol. All XRD measurements were carried out at scan speeds of 1° 2θ per minute, although slower scans (0.02° 2 θ) were often employed between 5° and 65° for higher resolution and peak separation. A cobalt K- α X-ray source was used throughout. Accessory mineral identification required grain size separation; however, efforts were primarily focused on the coarse sediment fraction. SEM backscatter electron measurements (BSE) were conducted to provide qualitative information about mineral compositional variability on a fine scale. These data in conjunction with XRD measurements were found to be especially useful for evaluation of both sulfide and silicate minerals, including compositional changes associated with diatom recrystallization reactions.

The magnetic properties of minerals are a highly useful means to examine the relative abundance and distribution of magnetite and pyrrhotite and overall redox conditions more generally. Accordingly, selected samples were examined using Princeton Corporation 3900 vibrating sample magnetometer to a maximum field of ± 1.2 T at roomtemperature. Saturation magnetization (M_S) was determined from hysteresis loops following high-field slope correction (0.8–1.2 T) based on the non-linear approach-to-saturation fitting method developed by Jackson and Solheid (2010). Magnetite weight percent was then determined by dividing sample magnetization by pure magnetite (92 Am²/ kg). Pyrrhotite weight percentage was determined by dividing sample magnetization by pure pyrrhotite (18 Am²/kg). Additional measurements at low-temperatures (20–300K) to identify characteristic magnetic transitions for magnetite (Verwey transition at ~120 K) and monoclinic pyrrhotite (Besnus transition at ~34 K) and confirm their presence were carried out with a superconducting quantum interference device (SQUID) magnetometer (Quantum Design MPMS-5S). All magnetic analysis was performed on approximately 100 mg of bulk sediment and carried out at the National Science Foundation Institute for Rock Magnetism at the University of Minnesota.

3. Results

3.1. Mineralogy

Sediment cores within the Deep Hole region (YL17U01-YL17U04) reveal broadly similar mineralogical composition, although some variability was noted with depth and location in individual cores. Near-vent sediment mineralization is largely composed of kaolinite and pyrite, with lesser amounts of smectite or boehmite, with smectite deeper in cores and more often associated with quartz or diatom fragments.

Progression away from sites of active venting display noteworthy abundance of amorphous silica, with sediment 30 m away (YL17U05) overwhelmingly dominated by diatomaceous silica, typical of near-surface sediments elsewhere in Yellowstone Lake (Shanks III et al., 2007). On-going detrital sedimentation from distal sources as well as localized vent sources adds to the mineralogical diversity of near and far-field vent mineral compositions. Thus, the very upper portions of some cores (YL17U02 and YL17U04) are characterized by the coexistence of diatomaceous (silica-rich) and kaolinite/boehmite (silica-poor) sediments. ROV observations at vents confirm the existence of hydrothermally sourced particles in the water column from vent exhalation events, as initially described by Fowler et al. (2019b). This may additionally account for minor amounts of smectite, kaolinite, and boehmite in reference core YL17U05. Lake-bottom currents transport these hydrothermal minerals to this off-site location.

Mineralogical differences between push cores may also vary as a result of vent specific differences in the temperature and chemistry of respective vent fluids, which can serve as primary constraints on the composition of minerals throughout the cores. Some of the differences reflect the degree of lake water mixing and cooling at the time of sampling as well as more fundamental differences in redox and pH caused by corresponding differences in H₂S and CO₂ in the vapor-rich hydrothermal fluids. It is not surprising, therefore, that mineralization of the primary vent sites are qualitatively different, especially involving abundance of sulfide and oxide minerals.

3.2. Chemical alteration

The major and trace element chemistry of variably altered sediment samples from the SI Deep Hole area of Yellowstone Lake is listed in Table 1. In general, samples from within or very near vent sites reveal Al $_2$ O $_3$ (20 to 28 wt%), SiO $_2$ (34 to 50 wt%) and H $_2$ O (9 to 12 wt%) in amounts broadly consistent with the abundant presence of kaolinite (Fig. 5). This is particularly apparent for sample YL17U02M, where SiO $_2$:Al $_2$ O $_3$:H $_2$ O wt% proportions are nearly identical to those of kaolinite. Immobile element ratios, especially involving Al $_2$ O $_3$ and TiO $_2$, indicate large scale mass and volume changes relative to the inferred protolith (Fig. 5). Similarly, Zr, Nb, Hf, and Ta tend to follow this same trend, with concentrations of these trace immobile elements increasing with increasing Al $_2$ O $_3$ (Table 1).

The relationship between river load sediment and sediment inferred to represent relatively unaltered sediment in the Deep Hole region suggests the combination of detrital riverine sediment and diatomaceous silica best represents the protolith prior to hydrothermal alteration (Fig. 5). As such, an assumed protolith may therefore be quantified utilizing identified proxy minerals in riverine sediment load such as lithological factors of feldspar and Fe-oxides minerals (Chaffee et al., 2007), as well as amorphous silica (Shanks III et al., 2007). Thus, mass loss, relative to the inferred protolith, overwhelmingly involves large scale removal of the sediment silica fraction, a result consistent with the elevated temperature, dilute composition and acidity of the vapor-dominated vent fluids (Fowler et al., 2019b) (Fig. 3).

Elevated $\rm H_2S$ concentrations of the hydrothermal vent fluid (Fig. 3) generally account for the elevated sulfur contents in the vent mineral deposits, although considerable variability is apparent owing to chemical

Table 1Chemical composition of hydrothermal vent deposits in the SI Deep-Hole region of Yellowstone Lake. Subsamples for analysis were obtained from ROV recovered push cores. Letters designate location in the core: T, M, and B, stand for: "top", "middle", and "bottom of cores, respectively, at designated locations.

	YL17U01B	YL17U02T	YL17U02M	YL17U02B	YL17U03B	YL17U04T	YL17U04B	YL17U05B
Na ₂ O	0.65	0.91	=	1.15	0.30	0.07	0.47	1.01
MgO	0.83	0.98	0.70	0.59	5.23	0.63	6.00	1.67
Al_2O_3	26.00	25.00	39.00	26.40	28.40	25.80	28.40	13.20
SiO ₂	49.90	40.78	39.25	34.60	45.25	33.90	41.60	61.60
P_2O_5	0.18	0.32	0.13	0.10	0.57	0.30	1.00	0.21
SO ₃ *	2.98	2.82	3.25	10.40	1.74	5.20	0.08	_
K ₂ O	0.69	0.59	0.26	0.36	0.20	0.41	0.22	1.06
CaO	0.60	0.67	0.18	0.42	1.25	0.52	1.75	1.36
TiO ₂	0.97	0.84	1.01	0.91	1.05	0.93	1.16	0.51
MnO	0.02	0.03	0.00	0.01	0.11	0.02	0.16	0.03
Fe_2O_3	5.52	10.20	2.92	20.20	6.08	13.90	8.74	3.26
H_2O	10.14	10.50	13.20	9.18	10.68	10.70	11.65	-
Total	99.00	93.70	99.95	104.40	100.90	92.50	101.00	83.90
Trace elem	ients (ppm)							
Ba	330.0	289.0	_	120.0	79.2	200.0	99.0	633.0
Li	3.3	0.9	_	3.0	1.0	1.1	4.4	0.5
Sr	119.0	119.0	_	48.7	61.5	84.5	68.0	266.0
Zr	337.1	298.7	-	371.0	267.0	271.0	329.7	185.1
Nb	27.6	23.1	-	26.7	19.6	23.2	23.5	16.3
Te	0.3	0.1	-	0.1	0.1	0.1	0.1	0.0
Hf	9.0	7.8	_	9.2	7.2	8.2	8.3	5.1
Ta	1.6	1.3	_	1.6	1.1	1.4	1.3	0.9
W	83.9	115.4	_	34.2	20.4	142.7	49.3	56.2

^{*} Measured by XRF, -Not measured, - Not detected, YL17U02M was measured entirely by XRF.

and physical factors unique to each core site (Figs. 3, 4). H₂S addition to unaltered sediment can be expected to form pyrite and/or pyrrhotite from Fe-bearing oxides in unaltered sediments. Pyrite is a common hydrothermal alteration mineral throughout YNP, and has been especially well described in the vapor-dominated region of the Y-11 drill hole (White et al., 1971; White et al., 1975; Fournier, 1989). Sediment derived iron, however, is difficult to identify unambiguously and may take several forms. Magnetite has been recognized in all cores, visually (SEM), mineralogically (XRD), and more quantitatively from magnetic data (low-temperature magnetism). Magnetic saturation measurements range from 0.001 to 0.087 Am²/kg (0.001–0.009 wt%), with higher values typically appearing in the top 3 cm of sediment (Table 2), suggesting detrital sources. Moreover, the magnetic signal indicative of pyrrhotite (Besnus transition) has also been revealed by the low temperature magnetitic data, at depth in core YL17U03-sample 1. The presence of pyrrhotite is not surprising as indicated by earlier samples from some of these same cores. Indeed, the earlier study by Fowler et al. (2019a) emphasized sulfur isotope applications and largely confirmed a magmatically derived source of sulfur for the pyrrhotite fraction in the hydrothermally altered SI Deep-Hole sediments. Although the vapor phase is both hot and acidic, the lack of ligands, such as chloride, limits Fe transport, resulting in Fe mineralization to a level limited largely by the availability of Fe from detrital sources.

3.3. Hydrogen isotopes

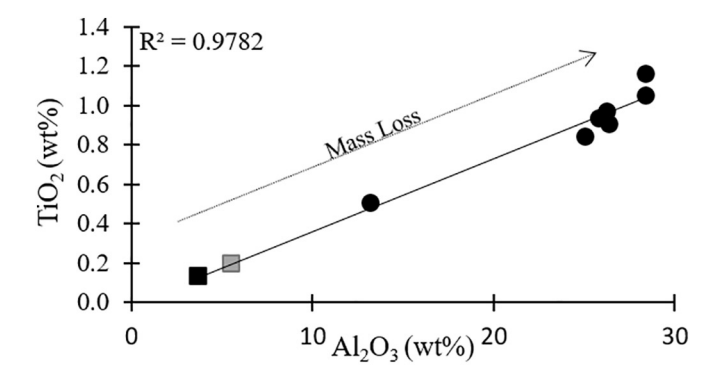
The hydrogen isotope composition of hydrothermally altered sediment samples range from -139 to -157%, with an average of -150%; up to 35% lighter than measured for coexisting vent fluid samples (Fowler et al., 2019b). Variability in the hydrogen isotope data, however, is still apparent, likely owing to core specific differences in chemical and physical conditions, which can cause slight but still significant differences in the abundance of hydrous secondary mineral phases (Table 3). The light δD values of the hydrothermally altered sediment are consistent with the formation of kaolinite (Gilg and Sheppard, 1996). A number of field, laboratory and theoretical studies have been conducted to measure the fractionation of hydrogen isotopes in the kaolinite water system (Sheppard et al., 1969; Lambert and Epstein, 1980;

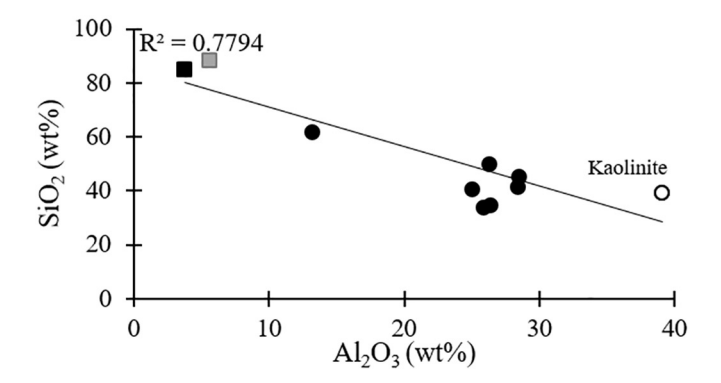
Marumo et al., 1980; Gilg and Sheppard, 1996; Méheut et al., 2007;). Not surprisingly, the diverse approaches and range of temperatures emphasized in these studies resulted in variability of the data and apparent magnitude in the relative abundance of hydrogen isotopes in kaolinite relative to a coexisting fluid, especially at relatively low temperatures. For the present study, we adopted data from Gilg and Sheppard (1996), which are experimental data focused on low to moderate temperatures and are in good agreement with field observations reported by Marumo et al. (1980). Sample YL17U02M, where kaolinite is the only hydrous alteration mineral present, has a δD of -155%, underscoring the magnitude of isotopic fractionation possible during acid metasomatism and kaolinite formation in the hydrothermally altered lake-bed sediments. A small subset of the hydrothermally altered sediment contained boehmite as well. In general, the limited data that are available for hydrogen isotope fractionation for the boehmitewater system (Graham et al., 1980) suggests relatively large fractionation, with the mineral considerably lighter than the fluid from which it formed at moderately low temperatures (~150 $^{\circ}$ C). Thus, the kaolinite and boehmite in hydrothermally altered sediment from the SI Deep-Hole can provide clues to the temperature of formation, when combined with constraints imposed by δD values of vent fluids and hydrogen isotope fractionation data.

As lake water in the Deep Hole region mixes with high enthalpy steam and then steam condensate, hydrogen isotope compositional variability of the circulating fluids results and this must be taken into account during mineralization reactions (Horita and Wesolowski, 1994) if formation temperatures are to be properly estimated from the isotopic composition of hydrous alteration phases (see below). As emphasized by Fowler et al. (2019b) steam addition can be quantified utilizing measured chloride values as a tracer. Conservative mixing of the inferred hydrothermal "endmember" yields a range of conditions under which kaolinite and associated minerals can form (Fig. 6).

4. Discussion

Observations based on the chemical and mineralogical analysis of hydrothermally altered sediments from the SI Deep-Hole vents confirm the extent of alteration resulting from interaction with steam-heated





- Stevenson Island vent mineralization
- Unaltered Yellowstone Lake sediment

□ River Sediment Load

 $\text{Fig. 5.}\,\text{Al}_2\text{O}_3$ versus TiO_2 concentrations (wt%) (Top) and SiO_2 versus Al_2O_3 concentrations (wt%) bottom) of hydrothermally altered sediments from the study sites in comparison with inferred unaltered Yellowstone Lake sediment (Shanks III et al., 2007) and Yellowstone river sediment (Chaffee et al., 2007). Data indicate that hydrothermal alteration results in an apparent increase in the immobile elements, TiO $_2$ and Al $_2\text{O}_3$, as well as trace immobile elements (see text), suggesting considerable mass loss, as indicated. The most altered samples approach a composition consistent with that of kaolinite (Bottom). The dissolution of diatomaceous silica with the extent of hydrothermal alteration plays a key role in this.

Table 2Variability in magnetic phase mineralogy and abundance in hydrothermally altered sediments sampled from Stevenson Island Deep Hole push cores (see text). Sample names refer to core number followed by subsample number. All push cores were obtained in 2017. Thus, "01–02" indicates YL17U01- sample 2.

Sample designator	Depth (cm)	Ms [Am ² /kg]	Magnetic phase	wt%
01-01	4	0.014	Magnetite	0.016
01-02	3.5	0.005	Magnetite	0.006
01-03	3	0.087	Magnetite	0.095
01-04	2.5	0.033	Magnetite	0.035
01-05	1	0.026	Magnetite	0.029
02-01	18	0.001	Magnetite	0.001
02-02	14.5	0.005	Magnetite	0.005
03-01	14	0.013	Pyrrhotite	0.072
03-02	11	0.002	Magnetite	0.002
04-01	13	0.001	Magnetite	0.001
04-02	12.5	0.003	Magnetite	0.004
05-01	1	0.04	Magnetite	0.044
05-02	10	0.008	Magnetite	0.008

Table 3Deuterium/Hydrogen isotope values of SI Deep Hole hydrothermal vent fluid* and altered sediment.

Sample	Vent Name	Type	Measure Temperature	δD
YL16F01	08152016-1	Fluid	63	-124
YL16F02	08152016-1	Fluid	86	-124
YL16F03	08152016-1	Fluid	112	-125
YL16F05	08162016-1	Fluid	94	-122
YL16F07	08162016-2	Fluid	140	-124
YL16F06	08162016-3	Fluid	101	-124
YL16F08	08172016-1	Fluid	126	-126
YL16F09	08172016-2	Fluid	92	-123
YL16F10	08172016-3	Fluid	97	-125
YL16F11	Vent 1	Fluid	130	-124
YL16F12	Vent 1	Fluid	112	-125
YL16F13	Vent 1	Fluid	83	-124
YL16F14	Vent 1	Fluid	149	-125
YL17F01	Vent 1	Fluid	150	-127
YL17F02	Vent 1	Fluid	146	-126
YL17F03	Vent 2	Fluid	142	-125
YL17F08	Vent 1	Fluid	128	-125
YL18F02	Vent 1	Fluid	118	-129
YL18F03	Vent 2	Fluid	66	-125
YL18F04	Vent 1	Fluid	70	-123
YL17U01	Vent 1	Sediment	_	-155
YL17U02T	Vent 1	Sediment	_	-157
YL17U02B	Vent 1	Sediment	_	-152
YL17INSERT	Vent 2	Sediment	_	-139
YL17U04T	Vent 2	Sediment	=	-156
YL17U04B	Vent2	Sediment	=	-141
VR2	Vent2	Sediment	-	-113

*Fluid chemical and hydrogen isotopic composition previously reported (Fowler et al., 2019b; Fowler et al., 2019c); (—) Not Measured **Lithified fragment not sediment sample from active yent.

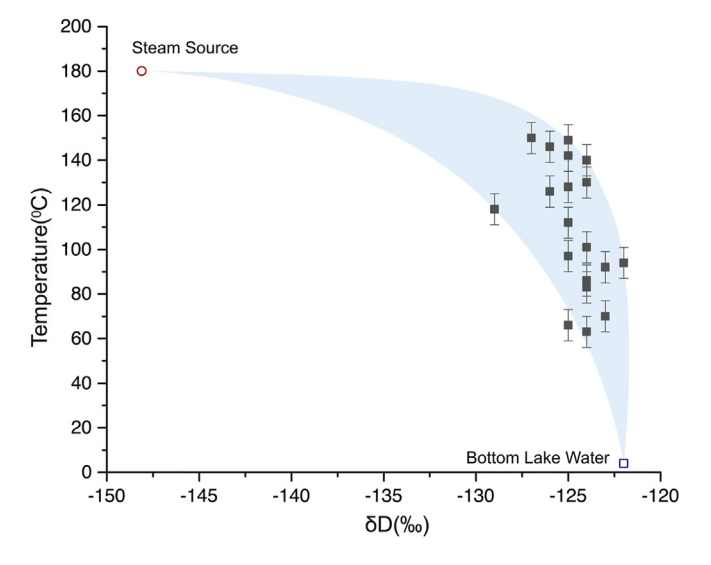
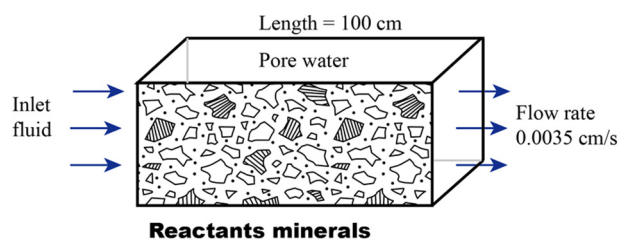


Fig. 6. The hydrogen isotope composition of hydrothermal vent fluids sampled in the Deep Hole region of Yellowstone Lake (symbols). Correlation of fluid temperature and measured hydrogen isotopic value determined by steam enthalpy calculations as reported in Fowler et al. (2019a). Conservative mixing between hydrothermally derived steam and bottom lake water is depicted by the upper boundary. Nonconservative mixing (conductive cooling) is represented by the lower bound, which is constrained by the lowest temperature vent fluids and their corresponding δD values, along with the lake water and steam source. The average variability of measure fluid temperature is \pm 7 °C. The temperature-dependent hydrogen isotope composition of hydrous alteration minerals (i.e., kaolinite) is dictated by heat loss phenomena.

lake water as these fluids discharge to the lake floor. Thus, the hydrothermal activity effectively transforms the lacustrine sediment into minerals stable at elevated temperatures and low pH conditions. The noteworthy concentrations of CO₂ and H₂S in the steam source



Am-Si; K-feldspar; Magneitite; Hematite

Fig. 7. Conceptual model depicting physical constraints used to simulate the interaction between steam derived condensate and lake water using the X1T RTM. The domain defined for the system is set at 10000 cm³. The inlet (source) fluid adds steam/condensate at 0.035 cm/s over the chosen cross-sectional area, which is scaled to the modeled dimensions from the hydrothermal fluid flux estimated for the entire SI Deep-Hole region (Sohn et al., 2019). The reaction temperature is 150 °C, which is generally consistent with the addition of 22% high enthalpy steam to each kg of 4°C lake water (Fowler et al., 2019b).

(Fowler et al., 2019a, 2019b, 2019c), however, provide a critical driving force for mineral alteration processes. Although the observed changes in the composition of the hydrothermally altered sediments qualitatively attest to the magnitude of heat and mass transfer that occurs in the sublacustrine vent system, application of a simple reaction path model to better understand the temporal evolution of the vapor-dominated hydrothermal system in the Deep Hole region on the floor of Yellowstone Lake. Such models have been used with increasing frequency and success to predict time series in the coexisting chemistry of minerals and fluids in hydrological and hydrothermal systems (Xu and Pruess, 2001; Navarre-Sitchler et al., 2011; Steefel et al., 2015; Yapparova et al., 2019).

4.1. Reaction path modeling

4.1.1. Conceptual development and imposed constraints

The reactive-transport module (X1T) of Geochemist Workbench (version 12.0.5) (Bethke and Yeakel, 2012) was used to perform mass transfer calculations simulating reaction between unaltered lacustrine sediment and gas-charged stream/lake water in time and space. The model assumes 1D flow through a compositionally simplified fresh sediment core and explicitly considers time series compositional and mineralogical changes for a fixed volume, as increasingly greater amounts of source (inlet) fluid enter the core, while a corresponding volume of reacted fluid leaves (Fig. 7). Accordingly, porosity increases because of mineral dissolution following a rate that is inherently surface-reaction controlled (see below). The volume of sediment and pore fluid that constitutes the domain for the reaction is 10,000 cm³, where mineral and pore fluid abundances were set at ~70 and ~ 30 vol%, respectively, broadly consistent with measurements made on least altered push cores recovered from the Yellowstone Lake Deep-Hole region (Fig. 4). The entire domain is discretized into 10 nodes to follow the fluid and mineralogical change with reaction progress, from inlet to exit. The

temperature and pressure of reaction were fixed at 150 °C and 12 bar, in agreement with observations made in the course of acquiring fluids discharging from Deep-Hole vents on the Lake floor (Fowler et al., 2019b). Finally, the recharge rate of inlet fluid was set to a value of 0.035 cm/s. This value was based on the volume of hydrothermal fluid that constitutes a plume of anomalously warm lake water recognized in the lake water column in the vicinity of the Deep-Hole region of Yellowstone Lake (Fowler et al., 2019b; Sohn et al., 2019). Scaling the flux of hydrothermal fluid needed to produce the plume over the Deep-Hole area to that of the much smaller domain used for the reaction transport model gives a value of 0.035 cm/s (Fig. 7). It is not our intent to model the entire Deep-Hole hydrothermal vent system, but rather to choose a small portion of the up-flow zone, on the scale of push core samples, to illustrate time-series changes that might apply to these samples.

The least altered core sampled and analyzed from the margins of the Deep-Hole vent field (YLU1705) was used to inform our choice of minerals and mineral abundances that relate to the starting, previously unaltered, composition of sublacustrine sediment that would be used for the simulation (Fig. 4). As noted previously, this core maintains a relatively non-disturbed appearance and reveals distinct sedimentary layering attesting to the accumulation of biological and detritally derived organic and inorganic mineral components by deposition from the water column in Yellowstone Lake. Compositional constraints indicate that this core contains abundant diatomaceous silica, feldspar fragments, and small but significant amounts of hematite and magnetite. Detailed mineralogical examination of the core reveals small amounts of numerous minor and trace minerals, but the RTM (reaction transport model) only considered the more abundant minerals. Thus, the idealized weight percentages of oxide components and volume percent minerals are summarized in Table 4. These minerals, both qualitatively and quantitatively, are broadly in agreement with so-called fresh surficial sediments in Yellowstone Lake (Balistrieri et al., 2007; Shanks III et al., 2007; Morgan et al., 2009b), although variability does exist, especially for regions of the lake closer to shorelines and further from the central basin, where complex depositional processes and local (glacial, volcanic) source material is to be expected. It is however, important to note that K-feldspar was used as a proxy for other igneous feldspar minerals containing CaO and Na₂O components, simplifying component numbers and thus facilitating convergence during computer simulations. Ca and Na-bearing phases have not been recognized in hydrothermally altered push cores, although secondary hydrous Al-bearing phases are typical and the proxy approach can be justified by focusing on the Al mass balance alone.

4.1.2. Reaction fluid source terms

Any model developed to assess time series hydrothermal alteration processes responsible for the temporal evolution of mineral and fluid reaction products must be cognizant of component sources contributing, both qualitatively and quantitatively, to the composition of the mobile fluid phase. As inferred above, there are two aqueous fluid sources that need to be considered: (1) the so-called inlet fluid, which represents the addition of condensate from the magmatically derived steam

Table 4Composition and abundance of minerals and component oxides used to represent unaltered sublacustrine sediment in the Deep Hole region of Yellowstone Lake. The phases and chemical composition were taken as input for reaction transport models and largely consistent with off-site core YL17U05 (see text).

	Chemical formula	Volume percentage for total (%)	Oxide	Weight percentage (%)
Amorphous -Silica	SiO ₂	33.60	SiO ₂	76.65
K-feldspar	$[K_2O-Al_2O_3-(SiO_2)_6]_{0.5}$	35.00	Al_2O_3	9.85
Magnetite	Fe ₂ O ₃ -FeO	0.70	K ₂ O	9.10
Hematite	Fe_2O_3	0.70	Fe ₂ O ₃	3.73
Porosity		30.00	FeO	0.68
Total		100		100

Table 5Initial (Yellowstone Lake water) and Inlet fluid (gas-rich steam condensate) for reaction transport simulation (see text). Concentrations are (mmol/kg) (Fowler et al., 2019b).

	Ca ²⁺	Cl ⁻	Fe ²⁺	HCO ₃	K ⁺	${\rm Mg}^{2+}$	Na ⁺	SiO ₂	SO ₄ ²⁻	pН
Initial				0.65						
	Ca ²⁺	Cl^-	Fe ²⁺	$CO_{2(aq)}$	K^{+}	Mg^{2+}	Na ⁺	SiO_2	$H_2S_{(aq)}$	pН
Inlet	0.13	0.12	1.57^*	66.00	0.04	0.104	0.39	0.21	5.00	$4.20^{\#}$

phase; and (2) lake water derived pore fluids. The steam phase and its condensate are best derived from constraints imposed by the temperature of fluid samples acquired at SI Deep-Hole vents (Fowler et al., 2019a; Fowler et al., 2019c). The Yellowstone lake water in the SI Deep Hole region was also sampled in-situ and reported in these same studies. The steam/condensate fluid is noteworthy for the abundance of magmatically derived gases- H₂S and CO₂. Visual observation at the vent sites indicates localized degassing of CO₂, characterized by gas streams in the water column, ultimately rising to the lake surface. The dissolved CO2 composition of pressurized, in-situ samples of vent fluid, together with corresponding temperature and pH, also in-situ data, are consistent with such an interpretation (Tan et al., 2017). H₂S, on the other hand, is present in abundance in the high-temperature vent fluid samples, but below dissolved concentrations sufficient for saturation (Fowler et al., 2019b). Thus, the inlet fluid and initial (pore) fluid (lake water) are largely similar in composition, with the exceptions being dissolved gases (H₂S and CO₂) and pH (Table 5). It is the introduction of these redox and pH controlling gases, however, that plays a critical role in mineral alteration processes.

4.1.3. Thermodynamic data for aqueous species and mineral reaction rate data

DBCreate (Kong et al., 2013) was employed to calculate stability constants for speciation and solubility data at 150 °C, 12 bar critical to the functionality and predictions from the X1T model. The thermodynamic data that are used with DBCreate, however, are primarily derived from the SUPCRT92 database (Johnson et al., 1992). Additionally, we adopted the Drummond (1981) formulation to calculate activity coefficients of CO_2 (aq) and H_2S (aq) in solution, while the internally consistent thermodynamic data presented by Tutolo et al. (2014) were employed for Al-bearing minerals and aqueous species, quartz, and H_4SiO_4 (aq). Silicic acid ionization constants and SiO_2 (am) thermodynamic data came from Busey and Mesmer (1977) and Gunnarsson and Arnorsson (2000), respectively. The extended Debye Hückel equation was used to calculate activity coefficients for charged aqueous species.

Rate constant data used in the model are most often calculated from kinetic and activation energy data 25 °C, which is then converted to rate expressions at higher temperatures using the Arrhenius equation

(Table 6). Accordingly, the kinetic reaction processes between fluid and minerals can be illustrated as follows (Lasaga, 1984):

$$r = A \cdot k_{25} \exp \left[\frac{-E_a}{R} \cdot \left(\frac{1}{T} - \frac{1}{298.15} \right) \right] \cdot \left[1 - \left(\frac{Q}{K} \right)^{\theta} \right]^{\eta}$$

where *r* refers to the reaction rate (positive for dissolution/negative for precipitation) [mol·kg $^{-1}$ ·s $^{-1}$], \hat{A} is the reactive surface area [cm²·g⁻¹], k_{25} refers to the reaction rate constant at 25 °C [mol·m⁻²·s⁻¹], E_a is the activation energy [kJ·mol⁻¹], T and R are the temperature [K] and ideal gas constant [J·mol⁻¹·K⁻¹], Q and K refer to the ion activity product and equilibrium constant of a specific mineral reaction, respectively, while θ and η are constants imposed by experimental data; but are set here to unity, as a consequence of the firstorder kinetics for the mineral-fluid systems studied. In the case of the kinetics of silica – water reactions, amorphous silica and guartz dissolution were calculated at 150 °C and steam saturation using the rate model and experimentally derived fit parameters developed by Rimstidt and Barnes (1980)(Table 6). Mineral reactive surface areas were estimated based on geometric analysis of minerals observed or separated from push cores. Mineral precipitation was expressed within an equilibrium framework related to mineral saturation state; that is mineral precipitation occurred whenever log Q/K values for a specific reaction exceeded unity.

Additionally, the reaction transport simulation included D/H isotopic fractionation factors for kaolinite-water (Gilg and Sheppard, 1996) and boehmite-water (Graham et al., 1980). Accordingly, model results predicted the effect of temperature and time on the H isotope composition of these hydrous alteration phases, which then could be compared with constraints imposed by the δD values of hydrous minerals actually measured at vent conditions.

4.1.4. Predicted time-series changes in pH and mineral alteration processes

Multicomponent reaction path modeling of hydrothermal alteration of sublacustrine sediments inferred to exist in and around SI Deep Hole vents, reveals large scale changes in chemical composition and mineralogy. Part of this can be accounted for by the high temperature (~150 °C), linked to the addition of high enthalpy steam (Fowler et al., 2019b), but the coexistence of $H_2S_{(g)}$ and $CO_{2(g)}$ in the steam phase, renders the mixture of steam condensate and lake water with which it mixes, not only acidic, but reducing. Model results predict a rapid decrease in pH from values somewhat typical of lake water to much lower values, which incrementally steps down to a steady value of ~4.8 after approximately 2 yrs. of reaction at a point of reference 55 cm into the 100 cm core (Fig. 8a). For consistency, we adopt 55 cm within the 100 cm long "core" as a reference point standardizing comparison for evaluation of time series changes in mineral and fluid components. Thus, the reported pH minima would occur sooner for portions of the core nearer the inlet and later, requiring longer reaction, for portions of the core

 Table 6

 Rate data and minerals kinetic parameters used in the reaction transport simulation.

	Rate constant at 150°C (mol/cm ² /s)	Surface area (cm ² /g)	Rate constant at 25° C (mol/m ² /s)	Activation Energy Ea (kJ/mol)
Amorphous -Silica	1.48715E-13 ^a	1E+3 ~ 1E+5 b	-	_
K-feldspar	1.43084E-13 ^c	1086 ^d	6.30957E-12 ^e	51.7 ^f
Magnetite	4.04539E-13 ^c	3810 ^g	1.12000E −10 ^h	30.1 ^h
Hematite	6.69880E-16 ^c	3810 ^g	4.07380E-10 ^f	66.2 ^f

⁽Rimstidt and Barnes, 1980).

^b (Zhang et al., 2011).

based on: Lasaga (1984) $k = k_{25} \exp\left[\frac{-E_a}{R}\left(\frac{1}{T_K} - \frac{1}{298.15}\right)\right]$. Where k_{25} is the constant at 25°C, Ea is the activation energy, R is the gas constant and T_K is the temperature (K).

d (Knauss and Copenhaver, 1995).

e (Helgeson et al., 1984) (Table 3, Experimental value at 25°C).

f (Palandri and Kharaka, 2004).

reactive surface area = $\frac{\text{surface area}}{\text{mass}} = \frac{4\pi r^2}{\rho \frac{4\pi}{r^3}} = \frac{3}{\rho r^4}$ assuming $r = 1 \times 10^{-4}$ cm, the density is 7.874 g/cm³;

h (White et al., 1994) (Table 4; pH = 5, temperature = 25°C, TAH magnetite).

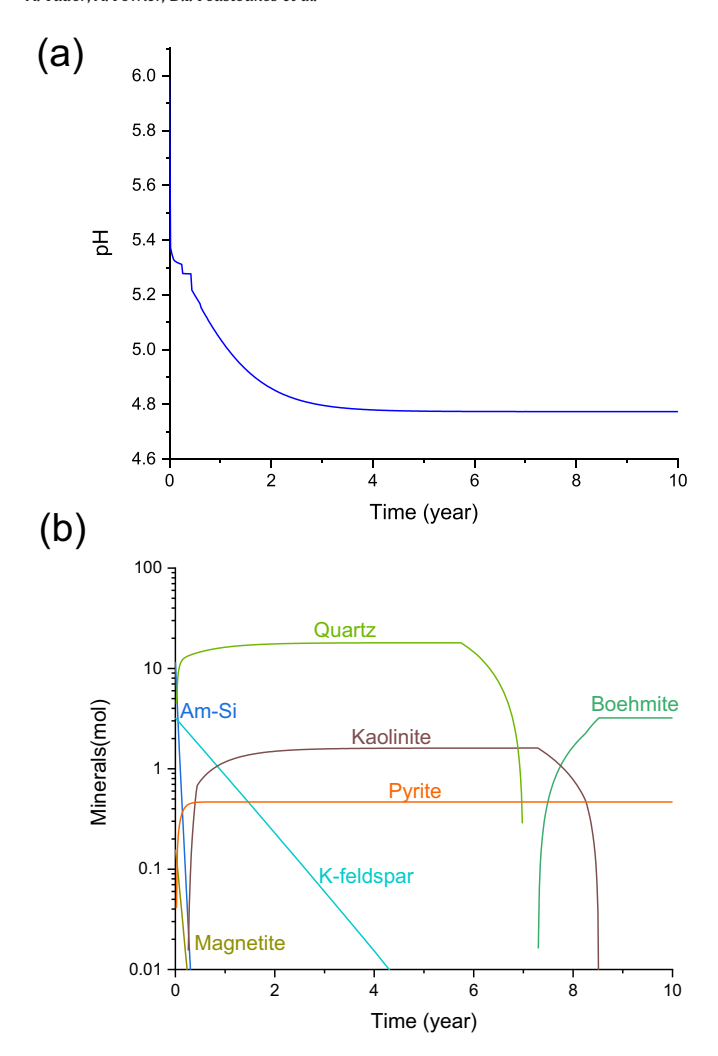


Fig. 8. (a) Reaction transport simulation of change in pH with time during the reaction of gas-bearing steam condensate, Yellowstone Lake water, and inferred lacustrine sediments (Table 4) at 150 °C. Hydrolysis of CO_{2 (aq)} provides an effective source of acidity, enhancing mineral alteration (Fowler et al., 2019b; Fowler et al., 2019c). Short term pH buffering shown during early-stage reaction is associated with feldspar and magnetite dissolution and then replacement by more stable minerals reactions (see text). The point of reference for these time series reactions occurs 55 cm in the modeled 100 cm sediment core. (b) Reaction transport simulation of time-series change in mineralogy as amorphous silica-rich (diatomaceous) sublacustrine first transforms to quartz and then undergoes near quantitative removal (dissolution) from the vent mineral system, while pyrite, kaolinite and diaspore are predicted to increase with increasing reaction progress. The predicted data underscore the reactivity of diatomaceous silica and the complete dissolution of quartz after approximately 7 years based on model constraints (see Table 4 and text). Boehmite-kaolinite is predicted to provide long term control on dissolved silica, in good agreement with push-core data and hydrothermal vent fluid chemistry. The point of reference for these time series reactions occurs 55 cm in the 100 cm modeled sediment core.

nearer the outlet. The short term buffering, where pH change is resisted, is primarily caused by feldspar replacement by kaolinite and also magnetite dissolution. In contrast, the longer term steady pH is caused chiefly by the relative lack of soluble cation bearing silicates and the continued influx of CO₂, the hydrolysis of which provides an effective source of H⁺. Interestingly, the long term pH values predicted by the RTM model (Fig. 8a) are in good agreement with in-situ pH values measured for hydrothermal fluids discharging from SI Deep Hole vents (Tan et al., 2017, 2020).

The decrease in pH does not occur in isolation but rather in combination with reducing conditions imposed by the influx of magmatically derived $H_2S_{(g)}$ and, of course, temperature increase. Indeed, it is the

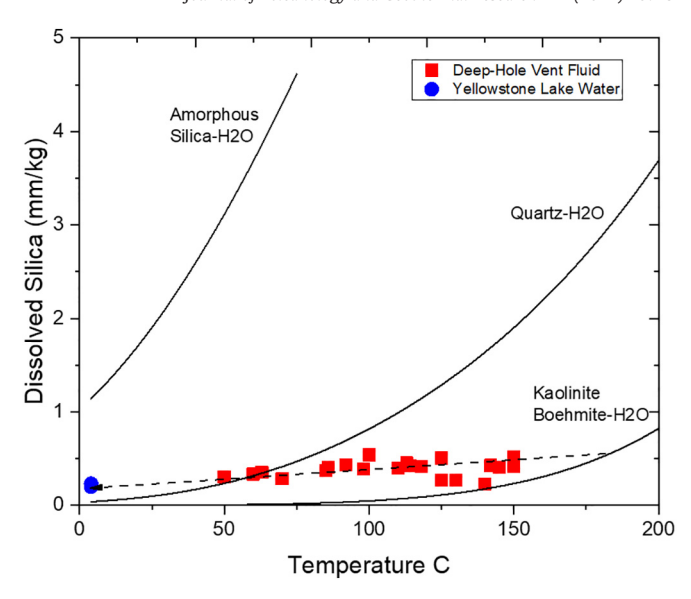


Fig. 9. Dissolved silica concentrations with temperature in hydrothermal fluids sampled from the SI Deep-Hole region (Fowler et al., 2019b). The mixing trend between silica in cold lake water (blue symbol) and high-temperature source fluids (red symbols) is apparent (dashed line). The high-temperature fluids approach kaolinite-boehmite (diaspore) saturation in a manner consistent with RTM predictions, confirming extensive reaction and silica depletion/dissolution from the sublacustrine protolith. Measured fluid silica concentrations are greatly undersaturated with respect to amount of the sublacustrine protolitation at all temperatures and quartz at temperatures above 74 °C, as expected from model calculations.

temperature (150 °C) that causes a dramatic increase in the rate of amorphous silica dissolution and transformation to quartz. At the reference location in the simulated core, the existence of diatomaceous silica is indeed short-lived (Fig. 8b), while quartz is predicted to remain stable for as long as approximately 7 years, buffering dissolved silica. Simultaneously, the replacement of K-feldspar by kaolinite conserves Al in the evolving vent mineralogy. With the continued influx of steam condensate and lake water, a reaction stage is achieved in which quartz solubility can no longer buffer dissolved silica and kaolinite formation gradually ceases, although kaolinite is predicted to long remain a stable alteration mineral. The late-stage coexistence of kaolinite and boehmite, where dissolved silica is predicted not to exceed approximately 0.2 mm/ kg is a critical point of reference. This is precisely the silica buffer reported by Fowler et al. (2019b) for SI Deep-Hole vent fluids, where dissolved silica increased slightly with increasing temperature and was observed to approach values consistent with kaolinite-boehmite equilibria at approximately 150 °C. Such conditions contrast sharply with dissolved silica concentrations buffered by amorphous silica (diatoms) or quartz (Fig. 9). Accordingly, the inferred (unaltered) sublacustrine protolith, characterized by a high SiO₂/Al₂O₃ ratio, is transformed with continued reaction with source vent fluid at elevated temperatures, into an alteration assemblage where the SiO₂/Al₂O₃ ratio is entirely reversed, in good agreement with the bulk chemistry and mineralogy observed in the SI Deep-Hole push cores (Fig. 5, Table 1). It is not surprising, therefore, that the vent mineral chemistry is also enriched in Ti and Zr, components that have been recognized to track with Al (Table 1) and exhibit little tendency to partition into the aqueous phase during hydrothermal alteration (Grant, 2005).

The relatively high $H_2S_{(g)}$ that characterizes steam and its condensate used as source fluid for the RTM simulation enhances magnetite reactivity, resulting in rapid replacement by pyrite (Fig. 8b). Pyrite is abundant in SI Deep-Hole vent deposits, where its formation has been interpreted to indicate both abiotic and biotic processes depending on depth within the hydrothermal up-flow zone, with altered sediments nearer the lake floor being more biologically influenced, while euhedral

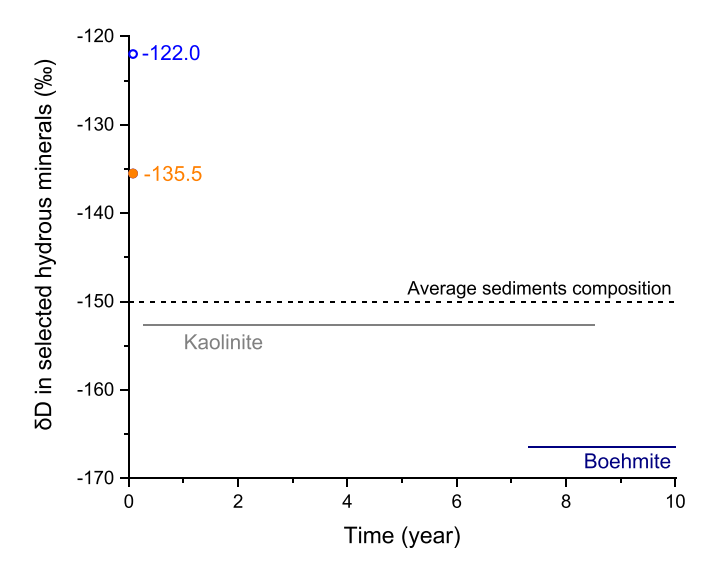


Fig. 10. Predicted δD of kaolinite and boehmite at 150°C in comparison with δD values from Yellowstone Lake water (-122.0%) and that inferred for the liquid condensate fractionated from the high enthalpy steam (-135.5%) (Horita and Wesolowski, 1994). The δD of Yellowstone Lake water is from Fowler et al. (2019b). Kaolinite and boehmite are produced from acid metasomatism of sublacustrine sediment by CO₂-rich source fluid. The relatively close correspondence between the measured δD (average bulk sediment composition) and that predicted for kaolinite, underscores the dominating influence of kaolinite in the sediment, while suggesting a temperature of formation of ~150 °C. The same is not the case for boehmite, suggesting its minor abundance in comparison to kaolinite or uncertainties in the temperature-dependent fractionation between boehmite and fluid at the modeled conditions. Hydrogen isotope fractionation data for Kaolinite and boehmite in the mineral-H₂O system are from Gilg and Sheppard (1996) and Graham et al. (1980), respectively.

(abiotic) pyrite is more typical of higher temperatures, where lake water ingress is less likely (Fowler et al., 2019a). Both pyrite generating processes, however, are likely mediated by the existence of more or less favorable kinetic pathways, even at elevated temperatures and pressures (Rickard and Luther, 2007). The present model cannot account for this and relies entirely on thermodynamic factors. Although the rates of magnetite sulfidation between natural and model systems may be very different, the process itself is vital for Fe cycling and the magnetitic character (see below) of hydrothermal vent minerals in the Deep-Hole hydrothermal system.

4.1.5. Controls on the hydrogen isotope composition of hydrous alteration phases

As noted, the RTM simulation includes data for the fractionation of hydrogen isotopes between mineral and aqueous fluid/vapor phases as a function of temperature and reaction progress. Thus, the D/H isotope composition of kaolinite and boehmite, the dominant hydrous alteration phases observed in the SI Deep-Hole vents, can be determined and compared with analogous data measured from push core samples. Model results, however, require knowledge of the hydrogen isotope composition of steam and liquid condensate for the inlet fluid. This fluid then undergoes mixing of Yellowstone Lake water coexisting with the inferred assemblage of previously unaltered sublacustrine sediment (Table 4). The δD composition of the steam source was estimated by Fowler et al. (2019b) and determined to be -148%. Taking explicit account of the fractionation of liquid water from the stream during condensation (Horita and Wesolowski, 1994), the liquid is calculated to be ~12.5% heavier than the vapor at the model temperature of 150 °C. Thus, the hydrogen isotope composition of the liquid "inlet" fluid for the model was set at a value of -135.5%.

Making use of these constraints, together with experimentally determined hydrogen fractionation data for kaolinite-water and boehmite-water (Graham et al., 1980; Gilg and Sheppard, 1996), δD

values for kaolinite and boehmite are predicted to be -152% and -168%, respectively (Fig. 10). Model results are in good agreement with δD for the kaolinite separates measured in hydrothermally altered push core sediments, while the predicted and measured values for boehmite agree far less well, suggesting a lack of equilibrium for this mineral at the assumed temperature, or compositional effects that can cause departure from the phase composition or mineralogy of that used for the determination of the fractionation data. Alternatively, the overwhelming abundance of kaolinite relative to boehmite in the vent minerals might account for these data as well. The good agreement for kaolinite, however, is encouraging in that it provides a level of confidence for the use of kaolinite as a means of assessing temperature in the SI Deep-Hole sublacustrine vent system. Although kaolinite formation is consistent with a formation temperature commonly recorded in the vent deposits- on both short and long-term time scales (Tan et al., 2017, 2020), vent fluid temperatures can be much more variable (Fig. 6). The inherently dynamic nature of venting of hot spring fluids likely accounts for this; where the ubiquitous presence of cold lake water, conductive cooling effects, and variability in the flux of hydrothermal source fluid through the sediment of low permeability, provide highly variable and complex paths of heat transfer.

4.1.6. Uncertainties implicit to RTM simulation predictions

Temperature variability inherent to hydrothermal upflow zones as described above provides one note of caution in interpreting too rigorously predictions involving the temporal and spatial variability in fluid chemistry and coexisting mineral alteration. Although uncertainty in temperature results in a series of downstream effects bearing on the accuracy of the predicted formation or dissolution of one mineral or another. This is especially true since temperature plays such an important role in affecting the magnitude of mineral reaction rate constants intrinsic to model predictions. Several other factors, however, are equally important in influencing model predictions. One involves the models lack of consideration of changes in the permeability of the hydrothermal upflow zone that necessarily affects the access of fluid to minerals in time and space. Here the 1D flow model assumed a constant volume for fluid flow in the 10⁴ cm³ "core" with no allowance for feedback between minerals and fluids intrinsic to mineral precipitation and dissolution, with clear implications for more or less void space with reaction progress. A related concern involves the accuracy of the assumption of a constant surface area of mineral reactants. This is a serious limitation in even the most sophisticated RTM simulations, based on years of experimental and field observations (White and Brantley, 1995; White et al., 2001), but likely made more challenging for the SI Deep-Hole vent system, owing to the abundance of diatomaceous silica in the hydrothermally altered sublacustrine sediments. The predicted rapid rate of diatomaceous silica dissolution and transformation to quartz plays a dominating role in the timing of a whole series of secondary mineralization events, such as those involving kaolinite and ultimately boehmite formation. The high surface area of diatom microfossils, however, likely changes in a non-linear way with reaction time, with implications for predicted silica release rates, specifically, and formation time for secondary silicates, more broadly. Although we have primarily focused on reaction rate uncertainties related to timedependent changes in amorphous silica surface area, similar concerns apply to aluminosilicate reaction rates, especially involving precipitation. As noted earlier, here we have assumed precipitation occurs upon saturation. The limited data in this regard that are available, however, often show that mineral precipitation, in particular, involves both nucleation and mineral growth, both of which can be complex functions of precursor mineral surface area, fluid chemistry, and saturation state (Nagy and Lasaga, 1993; Devidal et al., 1997). These and related studies underscore the need to better understand secondary mineral growth patterns in Yellowstone vent deposits. In the absence of studies of this sort, information critical to the determination of reactive surface area

will be ambiguous, precluding reaction path models from achieving their full potential.

4.2. Magnetization and hydrothermal alteration processes involving Fe

It has been demonstrated previously that despite the moderately high alteration temperatures and low pH of SI Deep-Hole hydrothermal fluids, Fe remains largely conservative with Fe provided from detrital and volcanic/sedimentary sources, which is then transformed into other Fe-bearing minerals more stable at the redox and pH conditions that prevail in hydrothermal upflow zones at the lake floor vents. The generally constant redox conditions, confirmed by in-situ chemical sensor deployments (Tan et al., 2017; Fowler et al., 2019b; Tan et al., 2020), are likely maintained by the influx of $H_2S_{(g)}$, which upon mixing with relatively small amounts of sulfate-bearing Lake water (Fowler et al., 2019b), achieves a steady state redox condition, which is reducing (Tan et al., 2017). Magnetite, which has been observed in push core samples and confirmed from magnetic measurements on samples from these same cores (Table 2), can be expected to be rendered unstable under such redox conditions, favoring replacement by pyrite, as follows:

Magnetite
$$+ H^+ + 5.5 H_2 S_{(g)} + 0.5 SO_4^{--} = 3 Pyrite + 6 H_2 O$$
 (2)

Pyrite replacement of magnetite is consistent with the reaction transport simulation (Fig. 8b), where the decrease in the abundance of magnetite is predicted to occur early in the sequence of mineral alteration processes. It is for this reason that the very existence of magnetite observed in the recovered push cores is of interest. This finding, however, needs to be assessed within the broader context of the magnitude of overall mass and volume change reactions that occur throughout the entire transformation process by which minerals highly unstable in moderately acidic and reducing hydrothermal fluids are transformed to more thermodynamically stable equivalents of the original mineral assemblage.

Mass and volume changes in the course of hydrothermal alteration processes can be calculated by use of a simple mass transfer reaction taking account of the change in the distribution of immobile elements and magnetite referenced to an assumed unaltered or starting composition, as follows:

$$C_i^a = \left(M^0/M^a\right)C_i^0 \eqno(3)$$

where C_i and C_i indicate the concentration of immobile component "i" in fresh and altered sediment respectively, whereas M^{o} stands for sediment mass before alteration and M ^a is the comparable mass after alteration (Grant, 2005). Here we use immobile elements in relatively fresh and altered cores to assess M^{o}/M^{a} , while assuming the distant push core, U05, represents the so-called "unaltered" reference against which the more altered sediments more closely associated with active stage hydrothermal alteration can be compared (Fig. 11). Accordingly, the normalized magnetization is predicted to be higher in altered samples with greater mass loss (e.g., with extensive amorphous silica dissolution) and would concentrate the abundance of magnetite, if magnetite behaved conservatively with the increase in alteration. In comparison with this ideal reference curve (Fig. 11), data indicate a decrease in average magnetization (average magnetite abundance in analyzed sediment samples) on the order of 29% in U01, 94% in U02, 96% in U03, and 96% in U04. The relatively high magnetite abundance in U01 is surprising and likely a consequence of the distortion and sediment loss of the core during core recovery (Fig. 4), although other factors may be involved.

It is important to note the role of pyrrhotite in contributing the magnetization measured for push core U03 (Fig. 11). Pyrrhotite is not common in the hydrothermally altered sediments recovered from the SI Deep-Hole region and tends to be located well below the lake sediment

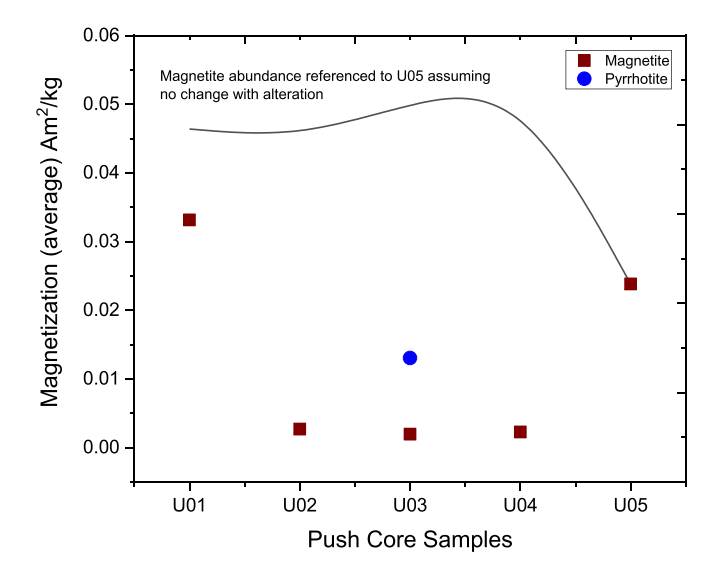


Fig. 11. Magnetization measurements of hydrothermally altered push cores from the SI Deep-Hole region compared with magnetization assuming the abundance of magnetite observed in reference core YL17U05 is unchanged with subsequent alteration and mass loss. Mass loss can be predicted from the magnitude of mineral dissolution and quantified from the change in immobile element concentrations between "fresh" (YL17U05) and more altered vent minerals. The low measured abundance of magnetite (red squares) suggests magnetite sulfidation and pyrite formation. Pyrrhotite in core sample YL17U03 is conspicuous and accounts for the anomalous magnetization intrinsic to this core sample.

surface. When observed, pyrrhotite is present as twinned crystals (Fig. 12) and provides evidence of the extent of redox heterogeneity that can exist on a fine-scale (Fowler et al., 2019a).

Numerous studies of paired redox couples in groundwater and low to moderate temperature hydrothermal systems have long demonstrated a lack of internal equilibrium. This is indicated by the noteworthy inconsistency of redox values predicted for individual redox couples as well as the overall disagreement between predicted and measured redox intensity (Grenthe et al., 1992; Stumm and Morgan, 1996; Stefansson et al., 2005). In a more qualitative sense, however, the variable redox condition provides support for a fluid (vapor) dominated hydrothermal vent environment, where the influx of H₂S (g) occurs at a sufficiently high rate to preclude more oxidizing conditions imposed by infiltration of lake water (oxygen and/or sulfate bearing) or development of more reducing conditions, possibly mediated by the breakdown of diatomaceous organic matter. It is this latter condition that might be particularly important for pyrrhotite formation and stability in the more deeply seated regions of the hydrothermally altered sediments in the SI Deep-Hole region of Yellowstone Lake.

Recent magnetic surveys of the northern basin of Yellowstone Lake involving aeromagnetic and autonomous underwater vehicle (AUV) observations (Bouligand et al., 2020) have helped to show how subsurface magnetization varies with rock type, temperature, and hydrothermal alteration of the rock, with implications for the effects of widespread fluid circulation on the magnetic character of subsurface lithologies. An important finding of the Bouligand et al. (2020) study was the recognition of decreased rock magnetization in the Deep-Hole region, where it is argued that demagnetization is associated with vapor condensation and mixing with lake water, with sulfidation of magnetite to pyrite, similar to that observed in the present study for the hydrothermally altered lake sediments. Moreover, Bouligand et al. (2020) correctly note that in the absence of an aqueous fluid (lake water, condensate), as might be inferred at depth in the Deep-Hole region, where the high enthalpy steam phase dominates, the magnetic character of the rocks through which the vapor passes would be expected to retain their magnetic

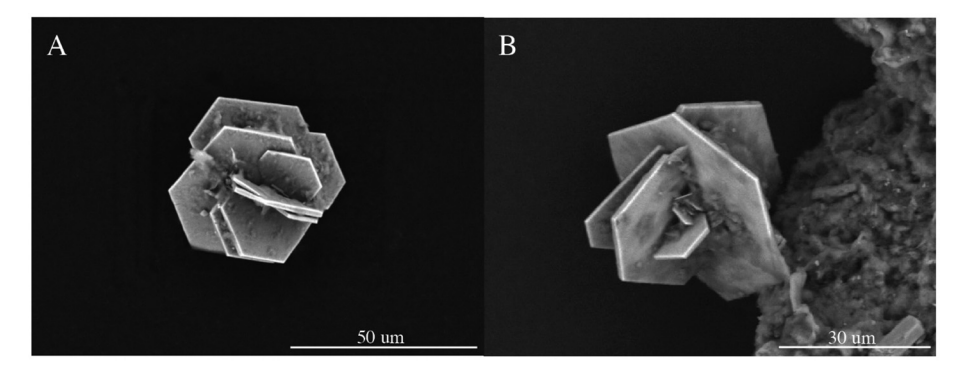


Fig. 12. SEM images of pyrrhotite showing crystallographic twinning. The samples were recovered from the bottom of vent 1 push core (YL17U03B), a site of active hydrothermal venting. Pyrrhotite is distinctive for the need for reducing conditions as well as its magnetic character, facilitating recognition in hydrothermally altered sediments.

character, as observed. Thus, rock/sediment magnetization studies on a range of scales can be shown to be powerful tools in understanding the temporal evolution of mass transfer reactions involving iron in sublacustrine hydrothermal systems.

5. Conclusions

Hydrothermal alteration associated with the reaction of vapor dominated fluids issuing from diffuse-flow vents on the floor of Yellowstone Lake, east of Stevenson Island was studied in push core samples recovered by ROV operations in 2017 and 2018. The core samples obtained penetrated ~5-22 cm into the vent deposits, with some samples directly associated with active exhalation of vent fluids at temperatures in excess of 150 °C at the lake floor pressure (~12 bar). Other core samples were offset 1 to 30 m from active vent sites, providing spatial and temporal information on the response of sublacustrine sediments to variable heat and mass transfer processes. With the exception of the 30 m offset core, which retained sedimentary layering and mineralogical evidence of only minor alteration, all near-vent push cores were highly altered, as indicated by variable degrees of brecciation and heterogeneously distributed mineralization dominated by kaolinite, pyrite and lesser quartz, pyrrhotite and boehmite. The extensive degree of acid metasomatism recorded in vent and near vent mineralogy and chemistry is entirely in agreement with previous studies of the chemical and isotopic composition of the vapor-dominated character of the vent fluids. These studies confirmed that high enthalpy steam mixes with lake water beneath the vent sites, providing heat and abundant quantities of $CO_{2(g)}$ and $H_2S_{(g)}$, rendering the mixture, hot, acidic and reducing, facilitating alteration of detritally and biologically derived components (diatomaceous silica) that can be inferred to represent unaltered Yellowstone Lake sediments.

Results of 1D reaction transport simulations provide key insight on the time series evolution of hydrothermal alteration processes and rates of mineral transformation likely in SI Deep-Hole vent deposits. At a temperature of 150 °C, model results indicate rapid dissolution of diatomaceous (amorphous) silica, followed in time by formation of quartz, kaolinite \pm boehmite, as increasingly greater amounts of acid generating CO2-rich fluid pass through the modeled core. The predicted and observed changes in vent deposit chemistry from high to low SiO2/ Al_2O_3 values with degree of alteration and reaction time are in good agreement, with both datasets emphasizing kaolinite formation and stability. Kaolinite-boehmite coexistence is consistent as well with the surprisingly low dissolved silica concentrations in SI Deep-Hole vent fluids. Moreover, the magnitude of hydrogen isotope fractionation between the predicted and measured vent fluid and kaolinite-rich substrate is consistent with kaolinite formation temperature of ~150°C.

Importantly, the predicted effectiveness of the transformation of amorphous silica to kaolinite results in substantial mass and volume change, potentially linking hydrothermal alteration of sublacustrine sediment to the formation of conical depressions and analogous bathymetric features intrinsic to SI Deep Hole, consistent with earlier models suggested for the formation of such features (Shanks III et al., 2007).

The abundant formation of pyrite observed in SI hydrothermal vent deposits and predicted from results of the 1D reaction transport simulation is best accounted for by sulfidation of magnetite. The observed decrease in magnetization with the extent of hydrothermal alteration is in agreement with this. On the other hand, for conditions sufficiently reducing, pyrrhotite stability is predicted, contributing further to the magnetic character of the altered sediments.

The vapor-dominated hydrothermal system on the floor of Yellowstone Lake serves as a natural laboratory to assess the effect of temperature, composition, and time on heat and mass transfer processes. It is likely that these same processes operate elsewhere in YNP, although below the land surface, at depths broadly equivalent to hydrostatic pressure in the Deep-Hole, the deepest part of Yellowstone Lake, where alteration reactions can achieve temperatures in excess of 150 °C.

Credit author statement

All authors have contributed equally.

Declaration of Competing Interest

The authors declare that they have no known competing financial interests or personal relationships that could have appeared to influence the work reported in this paper.

Acknowledgements

This work was funded by NSF grants EAR 1515377 and OCE 1434798 (W.E. Seyfried). D.I. Foustoukos acknowledges the NSF grant EAR 1761388. The Institute for Rock Magnetism is funded by the NSF Division of Earth Sciences, Instruments and Facilities program, and by the University of Minnesota. This is IRM contribution #2007. The authors thank Dave Lovalvo, the engineers onboard R/V Annie, and the Global Foundation for Ocean Exploration for their efforts that contributed to the successful outcome of the project. We also thank Dr. Rob Sohn and members of the HD-YLAKE research team for constructive advice and invaluable assistance during the three year field program. All work in Yellowstone National Park was completed under an authorized Yellowstone research permit (YELL-2018-SCI-7018).

References

- Balistrieri, L.S., Shanks III, W.C., Cuhel, R.L., Aguilar, C., Klump, J.V., 2007. The influence of sublacustrine hydrothermal vents on the geochemistry of Yellowstone Lake. In: Morgan, L.A. (Ed.), Integrated Geoscience Studies in the Greater Yellowstone Area: Volcanic, Tectonic, and Hydrothermal Processes in the Yellowstone Geoecosystem. U.S. Geological Survey Professional Paper, pp. 169–199.
- Bethke, C.M., Yeakel, S., 2012. The Geochemist's Workbench Release 9.0 Reaction Modeling Guide. Aqueous Solutions. LLC.
- Bouligand, C., Tivey, M.A., Finn, C.A., Morgan, L.A., Shanks III, W.C., Sohn, R.A., 2020. Geological and thermal control of the hydrothermal system in Northern Yellowstone Lake: inferences from high-resolution magnetic surveys. J. Geophys. Res. Solid Earth 125 (9), e2020JB019743.
- Busey, R.H., Mesmer, R.E., 1977. Ionization equilibriums of silicic acid and polysilicate formation in aqueous sodium chloride solutions to 300.Degree.C. Inorg. Chem. 16 (10), 2444–2450.
- Chaffee, M.A., Carlson, R.R., King, H.D., 2007. Environmental Geochemistry in Yellowstone National Park—Natural and Anthropogenic Anomalies and Their Potential Impact on the Environment USGS Professional Paper 1–29.
- Chiodini, G., Caliro, S., Lowenstern, J.B., Evans, W.C., Bergfeld, D., Tassi, F., Tedesco, D., 2012. Insights from fumarole gas geochemistry on the origin of hydrothermal fluids on the Yellowstone Plateau. Geochim. Cosmochim. Acta 89 (2012), 265–278.
- Christiansen, R.L., 2001. The Quaternary and Pliocene Yellowstone Plateau Volcanic Field of Wyoming, Idaho, and Montana. U. S. Geological Survey Professional Paper, p. 145.
- Cody, G.D., Ackerson, M., Beaumont, C., Foustoukos, D., Le Losq, C., Mysen, B.O., 2020. Revisiting water speciation in hydrous alumino-silicate glasses: a discrepancy between solid-state 1H NMR and NIR spectroscopy in the determination of X-OH and H2O. Geochim. Cosmochim. Acta 285, 150–174.
- Cotta, A.J., Enzweiler, J., 2012. Classical and new procedures of whole rock dissolution for trace element determination by ICP-MS. Geostand. Geoanal. Res. 36 (1), 27–50.
- Devidal, J.-L., Schott, J., Dandurand, J.-L., 1997. An experimental study of kaolinite dissolution and precipitation kinetics as a function of chemical affinity and solution composition at 150°C, 40 bars, and pH 2, 6.8, and 7.8. Geochim. Cosmochim. Acta 61 (24), 5165–5186.
- Drummond, S.E., 1981. Boiling and Mixing of Hydrothermal Fluids: Chemical Effects on Mineral Precipitation. Pennsylvania State University.
- Fournier, R.O., 1989. Geochemistry and dynamics of the Yellowstone National Park hydrothermal system. Annu. Rev. Earth Planet. Sci. 17, 13–53.
- Fowler, A.P.G., Liu, Q.-L., Huang, Y., Tan, C., Volk, M.W.R., Shanks III, W.C., Seyfried Jr., W.E., 2019a. Pyrite 834S and ∆33S constraints on sulfur cycling at sublacustrine hydrothermal vents in Yellowstone Lake, Wyoming, USA. Geochim. Cosmochim. Acta 265, 148–162
- Fowler, A.P.G., Tan, C., Cino, C., Scheuermann, P., Volk, M.W.R., Shanks III, W.C., Seyfried Jr., W.E., 2019b. Vapor-driven sublacustrine vents in Yellowstone Lake, Wyoming, USA. Geology 47 (3), 223–226.
- Fowler, A.P.G., Tan, C., Luttrell, K., Tudor, A., Scheuermann, P., Shanks III, W.C., Seyfried Jr., W.E., 2019c. Geochemical heterogeneity of sublacustrine hydrothermal vents in Yellowstone Lake, Wyoming. J. Volcanol. Geotherm. Res. 386, 106677.
- Gilg, H.A., Sheppard, S.M., 1996. Hydrogen isotope fractionation between kaolinite and water revisited. Geochim. Cosmochim. Acta 60 (3), 529–533.
- Graham, C.M., Sheppard, S.M., Heaton, T.H., 1980. Experimental hydrogen isotope studies —I. Systematics of hydrogen isotope fractionation in the systems epidote-H2O, zoisite-H2O and AlO (OH)-H2O. Geochim. Cosmochim. Acta 44 (2), 353–364.
- Grant, J.A., 2005. Isocon analysis: a brief review of the method and applications. Phys. Chem. Earth Parts A/B/C 30 (17-18), 997–1004.
- Grenthe, I., Stumm, W., Laaksuharju, M., Nilsson, A.C., Wikberg, P., 1992. Redox potential and redox reaction in deep groudwater systems. Chem. Geol. 98 (1–2), 131–150.
- Guice, G., Ackerson, M., Holder, R., George, F., Browning-Hanson, J., Burgess, J., Foustoukos, D.I., Becker, N., Nelson, W., Viete, D., 2021. Suprasubduction zone (SSZ) ophiolite fragments in the central Appalachian Orogen, USA: evidence for mantle and Moho in the Baltimore Mafic complex (Maryland). Geosphere. In presss.
- Gunnarsson, I., Arnorsson, S., 2000. Amorphous silica solubility and the thermodynamic properties of $\rm H_4SiO_4$ in the range of $\rm 0^0$ to $\rm 350^0$ C at P-sat. Geochim. Cosmochim. Acta 64 (13), 2295–2307.
- Helgeson, H.C., Murphy, W.M., Aagaard, P., 1984. Thermodynamic and kinetic constraints on the reaction rates among minerals and aqueous solutions: II. Rate constants, effective surface area, and the hydrolysis of feldspar. Geochim. Cosmochim. Acta 48 (12), 2405–2433.
- Horita, J., Wesolowski, D.J., 1994. Liquid-vapor fractionation of oxygen and hydrogen isotopes of water from the freezing to the critical temperature. Geochim. Cosmochim. Acta 58 (16), 3425–3437.
- Hurwitz, S., Lowenstern, J.B., 2014. Dynamics of the Yellowstone hydrothermal system. Rev. Geophys. 52 (3), 375–411.
- Jackson, M., Solheid, P., 2010. On the quantitative analysis and evaluation of magnetic hysteresis data. Geochem. Geophys. Geosyst. 11 (4).
- Johnson, J.W., Oelkers, E.H., Helgeson, H.C., 1992. SUPCRT92 a software package for calculating the standard molal thermodynamic properties of minerals, gases, aqueous species, and reactions from 1-bar to 5000-bar and 0°C to 1000°C. Comput. Geosci. 18 (7), 899–947.
- Johnson, S.Y., Stephenson, W.J., Morgan, L.A., Shanks III, W.C., Pierce, K.L., 2003. Hydro-thermal and tectonic activity in northern Yellowstone Lake, Wyoming. GSA Bull. 115 (8), 954–971.
- Knauss, K.G., Copenhaver, S.A., 1995. The effect of malonate on the dissolution kinetics of albite, quartz, and microcline as a function of pH at 70° C. Appl. Geochem. 10 (1), 17–33

- Kong, X.-Z., Tutolo, B.M., Saar, M.O., 2013. DBCreate: a SUPCRT92-based program for producing EQ3/6, TOUGHREACT, and GWB thermodynamic databases at user-defined T and P. Comput. Geosci. 51, 415–417.
- Lambert, S.J., Epstein, S., 1980. Stable isotope investigations of an active geothermal system in Valles Caldera, Jemez Mountains, New Mexico. J. Volcanol. Geotherm. Res. 8 (1), 111–129.
- Lasaga, A.C., 1984. Chemical kinetics of water-rock interactions. J. Geophys. Res. Solid Earth 89 (B6), 4009–4025.
- Marumo, K., Nagasawa, K., Kuroda, Y., 1980. Mineralogy and hydrogen isotope geochemistry of clay minerals in the Ohnuma geothermal area, northeastern Japan. Earth Planet. Sci. Lett. 47 (2), 255–262.
- Méheut, M., Lazzeri, M., Balan, E., Mauri, F., 2007. Equilibrium isotopic fractionation in the kaolinite, quartz, water system: Prediction from first-principles density-functional theory. Geochim. Cosmochim. Acta 71 (13), 3170–3181.
- Morgan, L.A., Shanks III, W.C., 2005. Influences of rhyolitic lava flows on hydrothermal processes in Yellowstone Lake and on the Yellowstone Plateau. In: Inskeep, W.P., McDermott, T.R. (Eds.), Geothermal Biology and Geochemistry in Yellowstone National Park: Proceeding of the Thermal Biology Institute Workshop. Yellowstone National Park, Wyoming, pp. 31–52.
- Morgan, L.A., Shanks III, W.C., Lee, G.K., Webring, M.W., 2007a. Bathymetry and geology of the floor of Yellowstone Lake, Yellowstone National Park, Wyoming, Idaho, and Montana. 2329-132X. Survey, US Geological.
- Morgan, L.A., Shanks III, W.C., Pierce, K.L., Lovalvo, D.A., Lee, G.K., Webring, M.W., Stephenson, W.J., Johnson, S.Y., Harlan, S.S., Schulze, B., 2007b. The floor of Yellowstone Lake is anything but quiet—New discoveries from high-resolution sonar imaging, seismic-reflection profiling, and submersible studies. In: Morgan, L.A. (Ed.), Integrated Geoscience Studies in the Greater Yellowstone Area: Volcanic, Hydrothermal and Tectonic Processes in the Yellowstone Geoecosystem. 1717. U.S.G.S. Professional Paper, pp. 1–35.
- Morgan, L.A., Cathey, H.E., Pierce, K.L., 2009a. The track of the yellowstone hotspot: multidisciplinary perspectives on the origin of the Yellowstone-Snake River Plain Volcanic Province. J. Volcanol. Geotherm. Res. 188 (1–3) pp. v-vi.
- Morgan, L.A., Shanks III, W.C., Pierce, K.L., 2009b. Hydrothermal processes above the Yellowstone magma chamber: large hydrothermal systems and large hydrothermal explosions. Geol. Soc. Am. Spec. Pap. 459, 1–95.
- Nagy, K.L., Lasaga, A.C., 1993. Simultaneous precipitation kinetics of kaolinite and gibbsite at 80°C and pH 3. Geochim. Cosmochim. Acta 57 (17), 4329–4335.
- Navarre-Sitchler, A., Steefel, C.I., Sak, P.B., Brantley, S.L., 2011. A reactive-transport model for weathering rind formation on basalt. Geochim. Cosmochim. Acta 75 (23), 7644–7667
- Palandri, J.L., Kharaka, Y.K., 2004. A Compilation of Rate Parameters of Water-Mineral Interaction Kinetics for Application to Geochemical Modeling. Geological Survey Menlo
- Raharjo, I.B., Allis, R.G., Chapman, D.S., 2016. Volcano-hosted vapor-dominated geothermal systems in permeability space. Geothermics 62, 22–32.
- Rickard, D., Luther, G.W., 2007. Chemistry of iron sulfides. Chem. Rev. 107 (2), 514–562.
 Rimstidt, J.D., Barnes, H.L., 1980. The kinetics of silica-water reactions. Geochim. Cosmochim. Acta 44 (11), 1683–1699.
- Rowe, J.J., Fournier, R.O., Morey, G.W., 1973. Chemical Analysis of Thermal Waters in Yellowstone National Park, Wyoming, 1960–65. US Government Printing Office.
- Schubert, G., Straus, J.M., Grant, M.A., 1980. A problem posed by vapour-dominated geothermal systems. Nature 287 (5781), 423–425.
- Sessions, A.L., Burgoyne, T.W., Hayes, J.M., 2001. Determination of the H3 factor in hydrogen isotope ratio monitoring mass spectrometry. Anal. Chem. 73 (2), 200–207.
- Shanks III, W.C., Alt, J.C., Morgan, L.A., 2007. Geochemistry of sublacustrine hydrothermal deposits in Yellowstone Lake: Hydrothermal reactions, stable isotope systematics, sinter deposition, and spire growth. In: Morgan, L.A. (Ed.), Integrated Geoscience Studies in the Greater Yellowstone Area: Volcanic, Hydrothermal and Tectonic Processes in the Yellowstone Geoecosystem. U.S.G.S. Professional Paper, pp. 205–234.
- Sheppard, S.M., Nielsen, R.L., Taylor, H.P., 1969. Oxygen and hydrogen isotope ratios of clay minerals from porphyry copper deposits. Econ. Geol. 64 (7), 755–777.
- Sohn, R., Harris, R., Linder, C., Lovalvo, D., Morgan, L., Seyfried Jr., W.E., Shanks III, W.C., 2017. The hydrothermal dynamics of Yellowstone Lake Eos Trans. AGU 98.
- Sohn, R.A., Luttrell, K., Shroyer, E., Stranne, C., Harris, R.N., Favorito, J.E., 2019. Observations and Modeling of a Hydrothermal Plume in Yellowstone Lake. Geophys. Res. Lett. 46 (12), 6435–6442.
- Steefel, C.I., Appelo, C.A.J., Arora, B., Jacques, D., Kalbacher, T., Kolditz, O., Lagneau, V., Lichtner, P.C., Mayer, K.U., Meeussen, J.C.L., Molins, S., Moulton, D., Shao, H., Šimůnek, J., Spycher, N., Yabusaki, S.B., Yeh, G.T., 2015. Reactive transport codes for subsurface environmental simulation. Comput. Geosci. 19 (3), 445–478.
- Stefansson, A., Amorsson, S., Sveinbjornsdottir, A.E., 2005. Redox reactions and potentials in natural waters at disequilibrium. Chem. Geol. 221 (3–4), 289–311.
- Stumm, W., Morgan, J., 1996. Aquatic Chemistry. John Wiley & Sons, New York.
- Tan, C., Cino, C.D., Ding, K., Seyfried, W.E., 2017. High temperature hydrothermal vent fluids in Yellowstone Lake: Observations and insights from in-situ pH and redox measurements. J. Volcanol. Geotherm. Res. 343, 263–270.
- Tan, C., Fowler, A., Tutor, A., Seyfried Jr., W.E., 2020. Heat and mass transport in sublacustrine vents in Yellowstone Lake, Wyoming: In-situ chemical and temperature data documenting a dynamic hydrothermal system. J. Volcanol. Geotherm. Res. 107043.
- Truesdell, A.H., White, D.E., 1973. Production of superheated steam from vapor-dominated geothermal reservoirs. Geothermics 2 (3), 154–173.
- Tutolo, B.M., Kong, X.Z., Seyfried Jr., W.E., Saar, M.O., 2014. Internal consistency in aqueous geochemical data revisited: applications to the aluminum system. Geochim. Cosmochim. Acta 133, 216–234.
- White, A.F., Brantley, S. (Eds.), 1995. Rev. Mineral. 31, 1-22.

- White, D.E., Muffler, L.J.P., Truesdell, A.H., 1971. Vapor-dominated hydrothermal systems compared with hot-water systems. Econ. Geol. 66 (1), 75–97.
- White, D.E., Fournier, R.O., Muffler, L.J.P., Truesdell, A.H., 1975. Physical Results of Research Drilling in Thermal Areas of Yellowstone National Park, Wyoming. Geological Survey, Reston, U. S., p. 0892.
 White, A.F., Peterson, M.L., Hochella, M.F., 1994. Electrochemistry and dissolution kinetics
- of magnetite and ilmenite. Geochim. Cosmochim. Acta 58 (8), 1859–1875.
 White, A.F., Bullen, T.D., Schulz, M.S., Blum, A.E., Huntington, T.G., Peters, N.E., 2001. Differential rates of feldspar weathering in granitic regoliths. Geochim. Cosmochim. Acta 65 (6), 847–869.
- Xu, T., Pruess, K., 2001. On fluid flow and mineral alteration in fractured caprock of magmatic hydrothermal systems. J. Geophys. Res. Solid Earth 106 (B2), 2121–2138.
- Yapparova, A., Miron, G.D., Kulik, D.A., Kosakowski, G., Driesner, T., 2019. An advanced reactive transport simulation scheme for hydrothermal systems modelling. Geothermics 78, 138–153.
- Zhang, D., Wang, Y., Zhang, W., Pan, J., Cai, J., 2011. Enlargement of diatom frustules pores by hydrofluoric acid etching at room temperature. J. Mater. Sci. 46 (17), 5665–5671.